R-Parity violating decay of a Tau-Sneutrino into Electron + Tau at CMS at $\sqrt{s} = 13$ TeV

von

Alex Siegfried Kreuzer

Bachelorarbeit in Physik

vorgelegt der

Fakultät für Mathematik, Informatik und Naturwissenschaften
der RWTH Aachen

angefertigt im

III. Physikalisches Institut A

im

Juli 2016

bei

Prof. Dr. Thomas Hebbeker

Eidesstattliche Versicherung

_____ _____

Name, Vorname Matrikelnummer (freiwillige Angabe)

Ich versichere hiermit an Eides Statt, dass ich die vorliegende Arbeit/Bachelorarbeit/ Masterarbeit* mit dem Titel

_____

_____

_____

selbständig und ohne unzulässige fremde Hilfe erbracht habe. Ich habe keine anderen als die angegebenen Quellen und Hilfsmittel benutzt. Für den Fall, dass die Arbeit zusätzlich auf einem Datenträger eingereicht wird, erkläre ich, dass die schriftliche und die elektronische Form vollständig übereinstimmen. Die Arbeit hat in gleicher oder ähnlicher Form noch keiner Prüfungsbehörde vorgelegen.

_____ _____

Ort, Datum Unterschrift

*Nichtzutreffendes bitte streichen

Belehrung:

§ 156 StGB: Falsche Versicherung an Eides Statt

Wer vor einer zur Abnahme einer Versicherung an Eides Statt zuständigen Behörde eine solche Versicherung falsch abgibt oder unter Berufung auf eine solche Versicherung falsch aussagt, wird mit Freiheitsstrafe bis zu drei Jahren oder mit Geldstrafe bestraft.

§ 161 StGB: Fahrlässiger Falscheid; fahrlässige falsche Versicherung an Eides Statt

(1) Wenn eine der in den §§ 154 bis 156 bezeichneten Handlungen aus Fahrlässigkeit begangen worden ist, so tritt Freiheitsstrafe bis zu einem Jahr oder Geldstrafe ein.

(2) Straflosigkeit tritt ein, wenn der Täter die falsche Angabe rechtzeitig berichtigt. Die Vorschriften des § 158 Abs. 2 und 3 gelten entsprechend.

Die vorstehende Belehrung habe ich zur Kenntnis genommen:

_____ _____

Ort, Datum Unterschrift

ABSTRACT

In this thesis a analysis of a R-parity violating tau sneutrino production and decay into the electron plus tau final state in proton-proton collisions at the LHC at CERN with a center-of-mass energy of $\sqrt{s} = 13$ TeV is presented. Here the tau sneutrino is considered as the lightest supersymmetric particle, which can decay into Standardmodell particles using the theory of baryon triality.

The data, used for this analysis, was recorded at CMS with an integrated luminosity of $\mathcal{L} = 2.7$ fb^{-1} in 2015 and is compared with Monte Carlo simulated background and signal samples. Criteria for the reconstruction of an electron and tau pair are analyzed and selected. Furthermore selection criteria and kinematic cuts are applied, to separate signal events from background events. As no significant deviations of data from the expected Standard Model processes are observed, limits on the cross section times branching ratio for a production of a tau sneutrino and decay into the electron plus tau final state are calculated for the used couplings.

KURZDARSTELLUNG

Im Rahmen dieser Bachelorarbeit wird eine Analyse zu einer R Paritäts verletzenden Produktion und Zerfall eines Tau-Sneutrinos in ein Elektron und Tau Paar im Endzustand in Proton-Proton Kollisionen am LHC am CERN vorgestellt. Das Tau Sneutrino ist hierbei das leichteste supersymmetrische Teilchen, das unter Annahme der Baryon Trialität in Standardmodell Teilchen zerfallen kann.

Für die Analyse weden Daten, die vom CMS Detektor bei einer Schwerpunktsenergie von $\sqrt{s} = 13$ TeV und einer integrierten Luminosität von $\mathcal{L} = 2.7$ fb^{-1} aufgezeichnet wurden, verwendet. Diese werden mit Monte Carlo Simulationen von Standardmodell Prozessen und des Signals verglichen. Dabei werden für die Rekonstruktion von Elektronen und Taus Auswahlkriterien untersucht und festgelegt. Weiterhin werden Auswahlkriterien und kinematische Schnitte zur Seperation von Signal- und Hintergrundereignissen diskutiert und angewandt. Da keine signifikante Abweichung der Messdaten von den Ereignissen des Standardmodells festgestellt wurden, wird eine Ausschlussgrenze für den Wirkungsquerschnitt der Erzeugung und des Zerfalls eines Tau-Sneutrinos in ein Elektron und Tau Paar im Endzustand für die benutzten Kopplungskonstanten berechnet.

CONTENTS

1 INTRODUCTION & THEORETICAL BACKGROUND

What are elementary particles? In physics a particle is a localized object, which is small in comparison to its containing system and can be described by several physical properties such as volume, mass or potential [1]. In addition, an elementary particle is a fundamental particle, which is not composed of other particles and therefore shows no behavior of containing a substructure [2].
One of the oldest and most popular concepts of an elementary particle is based on the ideas of the Greek philosopher Leukripp and his student Demokrit, who described an unimaginable small, indivisible element of matter, which was named "atom", meaning "indivisible" in Greek and being the fundamental element of all existing matter according to their theory [3].
In 1897 J.J. Thomson discovered the existence of electrons by observing a beam of charged particles with mass of a small fraction of atoms during experiments with cathode ray tubes. This observation violated the principle of indivisibility of atoms [3]. Until today an electron is considered as an elementary particle, showing no structure or components in experiments, but in the past century the atomic core was studied in various essential experiments or theoretical theses, like the experimental verification of neutrons by J. Chadwick or the postulate of quarks and gluons by Gell-Man [4].
So it is known today, that the atomic core consists of elementary particles, gluons and quarks, which are arranged in the Standard Model of Particle Physics (SM). This, in the 20th century developed model, describes the characteristics and interactions of elementary particles very precise, which was successfully verified in diverse experiments. In the last years and decades, new discoveries faced the SM with problems and ask for a "beyond Standard Model" like for instance cosmological phenomenons, which cannot be explained with matter arising from elementary particles in the SM. Therefore different modifications of the SM are discussed like Supersymmetry (SUSY) or the grand unified theory (GUT).
One of the major aims of experimental particle physics nowadays, is to find evidence for acceptance and rejection of such "beyond Standard Model" theories. In this theses data, taken at CMS in year 2015, is analyzed on a specific model, based on Supersymmetry.

1.1 STANDARD MODEL OF PARTICLE PHYSICS

Unless cited otherwise, this section is mostly based on reference [2] and [5]. In this thesis all values of variables are given in natural units.

The Standard Model of Particle Physics was developed mostly in the second half of the 20th century to describe the interactions and classifications of elementary particles in high energy particle physics.
All elementary particles are classified into two groups, determined by their spin attributes (spin quantum number or just spin). Particles with half integer spin are fermions and particles with integer spin are bosons.

1.1.1 *Gauge Bosons and Higgs Boson*

Bosons are divided between vector bosons with a spin of 1, called gauge bosons, and a scalar boson with a spin of 0, the Higgs boson.
The gauge bosons are defined in Gauge theory as force mediating particles or force carriers, that mediate electromagnetic, weak and strong fundamental interactions between respectively charged particles. A overview is given in Figure 1.

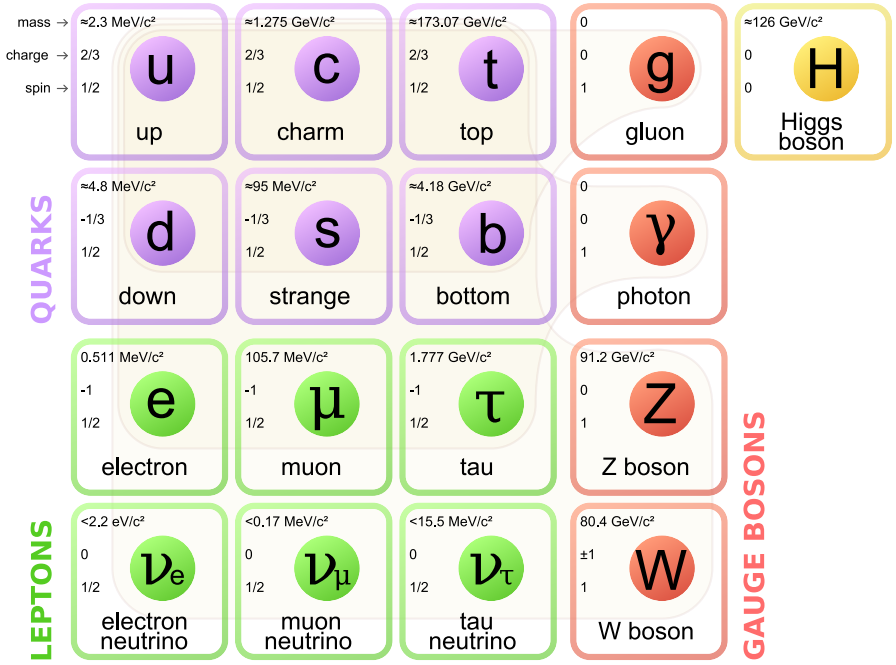

Figure 1: The Standard Model of Particle Physics with fermions (leptons and quarks) in the first three, gauge bosons in the fourth and Higgs boson in the fifth column. Retrieved from [6] .

The photon γ is the mediator of the electromagnetic force, which effects all electric charged particles and is described in the relativistic field theory of quantum electrodynamics (QED). Electromagnetic interactions have an infinite interaction range. The strength of coupling to a specific fundamental force or more precisely to specific gauge bosons is described by a factor, which describes the strength of the force exerted in a fundamental interaction, relative to the strong force in the SM.
Therefore the coupling strength is defined to be 1 for the strong interaction. Furthermore coupling strength factors are dependent on the energy scale of the given physical process, which results from energy-time uncertainty relation and virtual force mediating particles in QED. The coupling to electromagnetic interaction has a coupling strength order of $\alpha \approx 10^{-2}$ at energies of 1 GeV.

Gluons are massless, but color charged and couple to other gluons. They are the mediator of the strong interaction, which is the strongest force with a coupling strength order of $\alpha_S \approx 1$ at energies of 1 GeV but a range of 10^{-15} m. Every gluon is colored in a combination of one color and one anti-color. This combination with respect to three existing colors (red r, blue b and green g) and anti-colors ($\bar{r}, \bar{b}, \bar{g}$), leads to eight different gluon particles. Since gluons are color charged, they couple among themselves. Due to the self coupling, it is impossible to isolate a single gluon to propagate free in space. This specific attribute is called color confinement.

The third interaction of the SM is the weak force. The coupling strength has an order $\alpha_G \approx 10^{-5}$ at energies of 1 GeV and the interaction range is smaller than $\alpha_G < 10^{-15}$ m. Due to such a relatively small coupling strength, interactions of the weak force can only be observed, when strong or electromagnetic interactions are suppressed. The weak interaction has three different mediating gauge bosons: W^+, W^- and Z^0. The probability amplitude for mediation of forces via gauge bosons is proportional to a term, called propagator and given by $1/(q^2 - M^2)$ with relativistic particle momentum q and mass of the gauge boson M. The high mass of 80.39 Gev [2] for $W^\pm$ and 91.19 GeV [2] for Z^0 causes a small propagator and therefore a small coupling strength to the weak interaction, for values of q, which are not around the mass of the $W^\pm$ or the Z^0 boson.
Weak interaction is the only interaction, which not only mediates forces, but changes the quark flavor (for quark flavor see Section 1.1.2). For instance a electric negative charged down-quark changes into a electric positive charged up-quark under emission of a W^-, which decays into electron and anti-electron-neutrino. The $W^\pm$ boson is the mediator for charged current decays, changing the particle's electric charge, whereas the Z^0 boson is the mediator for neutral current decays without changing the particle's electric charge.

However gravity, as the most familiar force in everyday live, is not part of the SM. Although not yet found, the "graviton" should be the corresponding force-mediating particle to gravity [7]. Nevertheless the gravitational force has a coupling strength of around $\alpha_G \approx 10^{-41}$ for some GeV of energy scale and is completely negligible for high energy particle physics.

The property of weak interaction mediating particles to be massive, raises the question, how the masses of those particles are generated without violating gauge invariance and the important feature of renormalizability. To solve this problem a field theory with a symmetric (gauge invariant) potential $V(\Phi)$ was introduced and integrated into the SM. The minimum of $V(\Phi)$ is finite and non-zero, which results in a not gauge invariant ground state. The gauge symmetry is violated spontaneously. Fermions coupling to the ground state of this field $V(\Phi)$, generate mass terms for gauge bosons. Another result is an additional particle: the Higgs boson. This scalar particle couples to other particles proportional to their mass.

Table 1 shows the three fundamental forces of the SM, divided into their gauge bosons and their attributes. Although gravitation is no fundamental force of the SM as mentioned above, the gravitational force and the postulated graviton are listed as well for comparison.

Table 1: Fundamental forces, gauge bosons and their attributes in natural units with values for a energy scale around some GeV retrieved from [8]. The coupling strength factor is defined as the strength of the force exerted in a fundamental interaction relative to the strong force in the SM, normalized to be 1 for the strong interaction.

FUNDAMENTAL FORCE	GAUGE BOSON	COUPLING STRENGTH	RANGE (m)	CHARGE
strong	gluon g	1	$\approx 10^{-15}$	color charge
electromagnetic	photon γ	10^{-2}	∞	electric charge
weak	W^+, W^-, Z^0	10^{-5}	$< 10^{-15}$	weak charge
gravitational	graviton (postulated)	10^{-41}	∞	mass

1.1.2 *Quarks and Leptons*

All matter consists of elementary particles, which build nuclei, atoms and molecules like small building blocks of matter. The matter building particles belong to the fermions, which appear in two groups called quarks and leptons (see Figure 1). Each group is divided into three "generations" or "families", which consist of two particles each and differ in life-time and mass. All stable, ordinary matter in the universe consists of first generation particles. They are the lightest ones and stable: up- and down-quarks building protons and neutrons, building, together with electrons, atoms and molecules. Particles of higher generations are heavier and decay into other elementary particles with a certain probability. Table 2 shows the different quarks and leptons, divided into generations where the up- and down-quark belongs to the first generation, the charm- and strange-quark to the second generation and the top- and bottom-quark to the third generation. Quarks exist in six different flavors, two flavors each generation which differ in electric charge, mass and quantum numbers (as weak isospin T_3, baryon number B, strangeness S, etc. [8]).
They are charged with one color and they only add up in combinations of colorless particles. These composite particles are called hadrons, which are divided into mesons and baryons. Mesons consist of one quark with color and one anti-quark with the corresponding anti-color. Baryons consist either of three quarks with color or three anti-quarks with anti-color. In case of baryons, the single quarks have to belong to different colors, whereas three different colors or anti-colors result colorless. Being the only fermions, which carry color charge, quarks are the only particles besides gluons, interacting via the strong interaction. At high energies quarks do not disengage and cannot propagate free in space, but a new quark-antiquark pair appears in between, resulting in two mesons.
Also carrying fractional electric charge in units of the elementary charge e and weak isospin T_3, quarks additionally interact via electromagnetic and weak interaction. Though mesons and baryons are composed of quarks of different flavors, they have integer charge.
As mentioned above, also leptons appear in three generations (see Table 2) with one electric charged lepton of e^- (or e^+ for anti-leptons) per generation: the electron e, muon μ and tau τ. In addition, every generation has its corresponding non electric charged particle, called neutrino.

Quarks and leptons have the property of chirality, which is important regarding their interaction to weak force and therefore possible decay processes. Chirality describes the property of the particle's wave function under P-parity transformation, dividing into symmetric and antisymmetric parts of the wave function. Generally, P-parity describes the properties of particle's wave functions under parity transformation, which flips in the sign of one spatial coordinate. The crucial attributes here are the quantum numbers of isospin I and weak isospin T_3.
Fermions with negative chirality, called left-handed fermions, have isospin $I = 1/2$ and can be assigned to doublets with weak isospin $T_3 = \pm 1/2$ that behave the same way under weak interaction. For example, up-type quarks (u, c, t) have $T_3 = 1/2$ and always transform into down-type quarks (d, s, b), which have $T_3 = -1/2$ and vice versa. A quark never decays weakly into a quark of the same isospin.
Analogous rules apply for left-handed leptons, which exist as doublets containing a (e^-, μ^-, τ^-) with $T_3 = -1/2$ and a neutrino $(\nu_e, \nu_\mu, \nu_\tau)$ with $T_3 = 1/2$.
Fermions with positive chirality (also called right-handed fermions) have spin $T = 0$ and form singlets that do not interact weakly. Table 3 shows the classification of quark and leptons into right-handed singlets and left-handed doublets.

Table 2: Elementary particles and their attributes in natural units with values from [9] and [2] unless not cited otherwise.

PARTICLE CLASS			SPIN	MASS (GeV)	ELECTRIC CHARGE (e)	COLOR CHARGED
quarks	1. gen.	up u	1/2	$(2.3^{+0.7}_{-0.5}) \cdot 10^{-3}$	$+2/3$	✓
		down d	1/2	$(4.8^{+0.5}_{-0.3}) \cdot 10^{-2}$	$-1/3$	✓
	2. gen.	charm c	1/2	1.275 ± 0.025	$+2/3$	✓
		strange s	1/2	$(95 \pm 5) \cdot 10^{-2}$	$-1/3$	✓
	3. gen.	top t	1/2	173.2 ± 0.9	$+2/3$	✓
		bottom b	1/2	$4.1 - 4.4$	$-1/3$	✓
leptons	1. gen.	e	1/2	$5.111 \cdot 10^{-4}$	-1	X
		ν_e	1/2	$< 2 \cdot 10^{-9}$ [8]	0	X
	2. gen.	μ	1/2	0.106	-1	X
		ν_μ	1/2	$< 1.9 \cdot 10^{-4}$ [8]	0	X
	3. gen.	τ	1/2	1.777	-1	X
		ν_τ	1/2	$< 3.5 \cdot 10^{-2}$	0	X
gauge bosons		gluon	1	0	0	✓
		photon γ	1	0	0	X
		W^+	1	80.39 ± 0.26	$+1$	X
		W^-	1	80.39 ± 0.26	-1	X
		Z^0	1	91.19 ± 0.01	0	X
Higgs boson			0	125.09 ± 0.24 [10]	0	X

Table 3: Doublets of left-handed (denoted by a L) and singlets of right-handed (denoted by a R) fermions.

	DOUBLETS ($T_3 = 1/2$)	SINGLETS ($T_3 = 0$)
LEPTONS	$\begin{pmatrix} \nu_e \\ e \end{pmatrix}_L \begin{pmatrix} \nu_\mu \\ \mu \end{pmatrix}_L \begin{pmatrix} \nu_\tau \\ \tau \end{pmatrix}_L$	$(e_R^-), (\mu_R^-), (\tau_R^-)$
QUARKS	$\begin{pmatrix} u \\ d \end{pmatrix}_L \begin{pmatrix} c \\ s \end{pmatrix}_L \begin{pmatrix} t \\ b \end{pmatrix}_L$	$(u_R), (d_R), (c_R), (s_R), (t_R), (b_R)$

1.2 SUPERSYMMETRY

Even though the Standard Model describes elementary particles and the fundamental interactions very precise, there are phenomenons that cannot be explained by the SM, like gravitational interactions. Another problem is caused by dark matter. The observation of gravitational lensing effects and galaxy rotation curves in astrophysics lead to the assumption, that only about 5% of the matter in our universe consist of "ordinary" SM matter. About 26% of our universe consists of dark matter and about 69% of dark energy [11]. One of the most popular and thoroughly investigated extension of the SM is "supersymmetry" (SUSY), which makes answers for problems beyond the SM possible.

1.2.1 *Fundamentals*

The essential point of supersymmetry is the possibility to associate a bosonic particle to a fermionic particle and vice versa. Each particle of one group is associated with a particle from the other, known as the superpartner, which differs in spin. Besides the differing spin, superpartners must have same mass and internal quantum numbers in theory. Due to the fact that no supersymmetric particle was observed yet, supersymmetric particles must have greater masses than SM-particles, which leads to a broken symmetry. The Minimal Supersymmetric Standard Model (MSSM) is the theory of the simplest spontaneously broken symmetry and could solve many of the "physics beyond the Standard Model" problems like dark matter.
Gauge anomalies appear when adding a fermionic partner of the Higgs, requiring to add a second Higgs doublet to the model. Therefore in MSSM another Higgs doublet is added to the SM. Subsequent a superpartner is assigned to every SM particle, where the SM particle and its superpartner differ in spin by a half-integer. Similar to SM multiplets (see Table 3), which represent parts of particle eigenstates, supermultiplets contain SM and MSSM particles. Table 4 shows the supermultiplets of the MSSM. The bosonic superpartners of fermions

Table 4: Chiral- and gauge supermultiplets in the MSSM with values from [12]. Left-handed particles are sorted into doublets and right-handed particles into singlets.

CHIRAL SUPERMULTIPLETS				GAUGE SUPERMULTIPLETS		
NAME		SPIN 0	SPIN 1/2	NAME	SPIN 1/2	SPIN 1
sqarks, quarks (3 generations)	Q	$(\tilde{u}_L \quad \tilde{d}_L)$	$(u_L \quad d_L)$	gluino, gluon	$\tilde{g}$	g
	$\overline{u}$	$\tilde{u}_R$	u_R	winos, W-boson	$\tilde{W}^{\pm} \quad \tilde{W}^0$	$W^{\pm} \quad W^0$
	$\overline{d}$	$\tilde{d}_R$	d_R	binos, B-boson	$\tilde{B}^0$	B^0
sleptons, leptons (3 generations)	L	$(\tilde{\nu} \quad \tilde{e}_L)$	$(u_L \quad d_L)$			
	$\overline{e}$	$(\tilde{\nu} \quad \tilde{e}_L)$	$(\nu \quad e_L)$			
Higgs, Higgsinos	H_u	$(H_u^+ \quad H_u^0)$	$(\tilde{H}_u^+ \quad \tilde{H}_u^0)$			
	H_d	$(H_d^- \quad H_d^0)$	$(\tilde{H}_d^- \quad \tilde{H}_d^0)$			

are called sqarks and sleptons, differing in name by a preposed "s", superpartners of bosons end with "-ino". Superpartners are marked by a tilde. For instance, the tau sneutrino $\tilde{\nu}_\tau$ is the superpartner of the tau neutrino.

1.2.2 *R-Parity Motivation*

R-parity is a concept in SUSY. In the MSSM the baryon number B and the lepton number L are no longer conserved. A consequence of lepton and baryon number violation would be for instance a rapid proton decay within 10^{-2} s as a result of an odd number of superparners interacting. Since such a decay is excluded by experimental measurements, a new parity was introduced. The R-parity is defined by

$$P_R = (-1)^{(3B+L+2S)} \tag{1}$$

whereas S is the particle's spin. The multiplicative quantum number is $P_R = +1$ for SM particles and $P_R = -1$ for MSSM particles.
A result of conserved R-parity is, that supersymmetric particles can only be produced in even numbers and decay in a SM-particle-MSSM-particle pair. One very important result is, that the lightest SUSY particle (LSP) would be stable. Since the LSP was not observed yet, it is to consider the LSP being electric neutral and only weakly interacting. It is therefore a potential candidate for dark matter.

1.2.3 *R-Parity Violation*

Using the supermultiplets of Table 4, a potential in MSSM with supersymmetric components can be grouped to a superpotential [13]. These terms contain lepton number violating (LNV) as well as baryon number violating (BNV) triliniar terms

$$W_{LNV} = \epsilon_{ab}\left[\frac{1}{2}\lambda_{ijk}L_i^a L_j^b \overline{E}_k + \lambda'_{ijk}L_i^a Q_j^{xb}\overline{D}_{kx}\right] \tag{2}$$

$$W_{BNV} = \frac{1}{2}\epsilon_{xyz}\lambda''_{ijk}\overline{U}_i^x \overline{D}_j^y \overline{D}_k^z \tag{3}$$

With L, Q denoting lepton- and quark-superdoublets, $\overline{E}, \overline{U}, \overline{D}$ standing for electron-like and up/down-like quark-singulets, where i, j, k symbolize generation indices. The supermultiplets are listed in Table 4. The parameters λ, λ' and λ'' (Yukawa couplings) denote the coupling strengths of the respective interactions between the super fields. It is convenient to lower and raise spinor indices with ϵ-tensors like ϵ_{ab} and ϵ_{xyz}.
In this analysis a R-parity violating model is considered, whereas the stability of a proton is explained by baron triality [14], which allows lepton number violating terms, but forbids baryon number violating terms. Due to R-parity violation, the LSP is able to decay into SM particles, leading to final states, which are experimentally approachable.
In this analysis the tau sneutrino is considered as the LSP and the decay of a tau sneutrino into a electron plus tau final state is studied. Detailed information and values, which were used to simulate the signal of these model of R-parity violation, is discussed in Section 3.1.

2 THE EXPERIMENT

The data used for this analysis is recorded with the Compact Muon Solenoid (CMS) detector, which is an experiment at the Large Hadron Collider (LHC) at the European Organization for Nuclear Research (CERN). The data events were recorded in proton-proton collisions at a center-of-mass energy of $\sqrt{s} = 13$ TeV and a integrated luminosity of about 2.7 fb^{-1} at CMS during the data taking in 2015 .

2.1 THE LARGE HADRON COLLIDER

The LHC is a circular particle accelerator with 26.7 km circumference [15]. It is the latest and biggest part of CERN's accelerator complex, which is a succession of accelerators increasing the particle energies (see Figure 2). Seven experiments are connected to the LHC, whereby ALICE, ATLAS, CMS and LHCb are the major ones. The main goals of the LHC, which is in operation since the end of 2009, is to help answer many unanswered questions of the Standard Model of particle physics. Especially the origin of mass, the theory of supersymmetry, dark matter and the imbalance of matter and anti-matter, which lead to our universe, are core points of questions, which lead to the design of the LHC. They may be answered by these most powerful particle accelerator ever build.

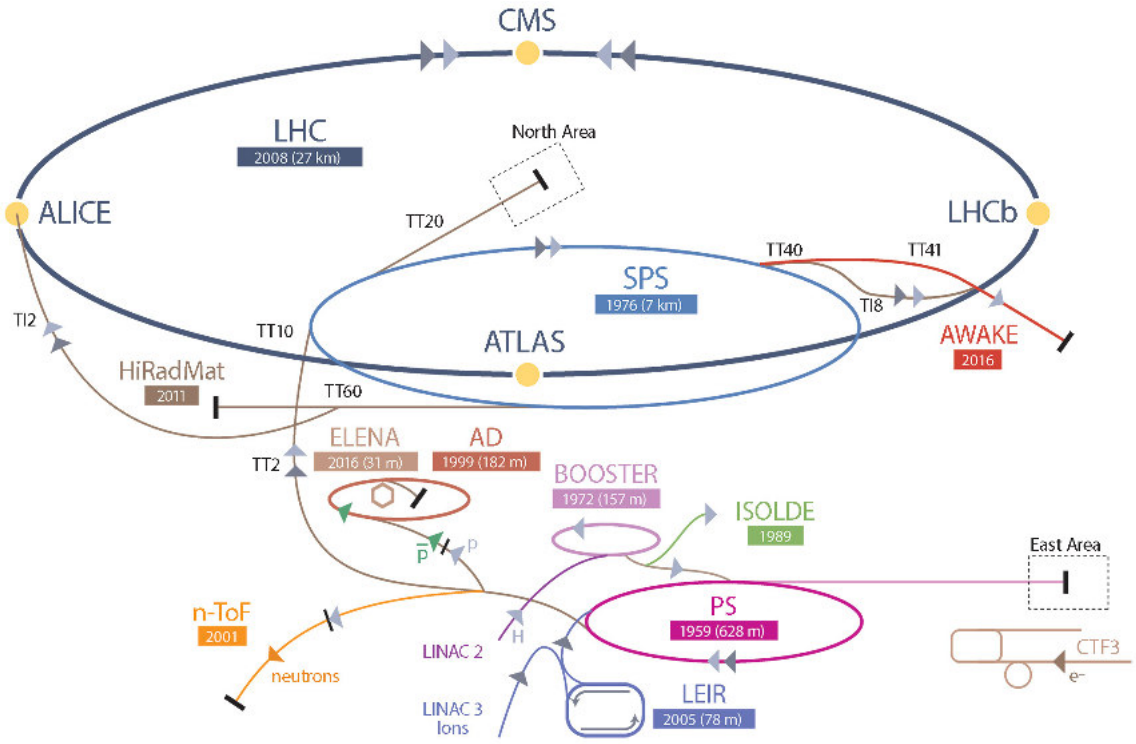

Figure 2: Schematic picture of the injector chain for the LHC at the CERN's accelerator complex. Extensions of the accelerator complex are colored distinguishly and labled with the date of their completion. Retrieved from [16].

2.2 THE COMPACT MUON SOLENOID

Unless cited otherwise, this section is mostly based on reference [17] and [18].

With around 14000 tonnes, about 15 meters diameter and 21.5 meters length, the Compact Muon Solenoid (CMS) is the experiment with the highest mass density at the LHC. It was designed to detect and measure decay products from proton-proton, proton-ion or heavy ion collisions with various different sub detectors. It is distinguished between detectors in the so called "Barrel", arranged parallel to the beam pipe, and flat detectors covering the openings of the barrel, which are called the "Endcaps". Figure 3 shows a schematic profile of the barrel with the different sub detectors layered around the collision point. The interaction of different kind of particles within the sub detectors are shown and their trajectories marked.

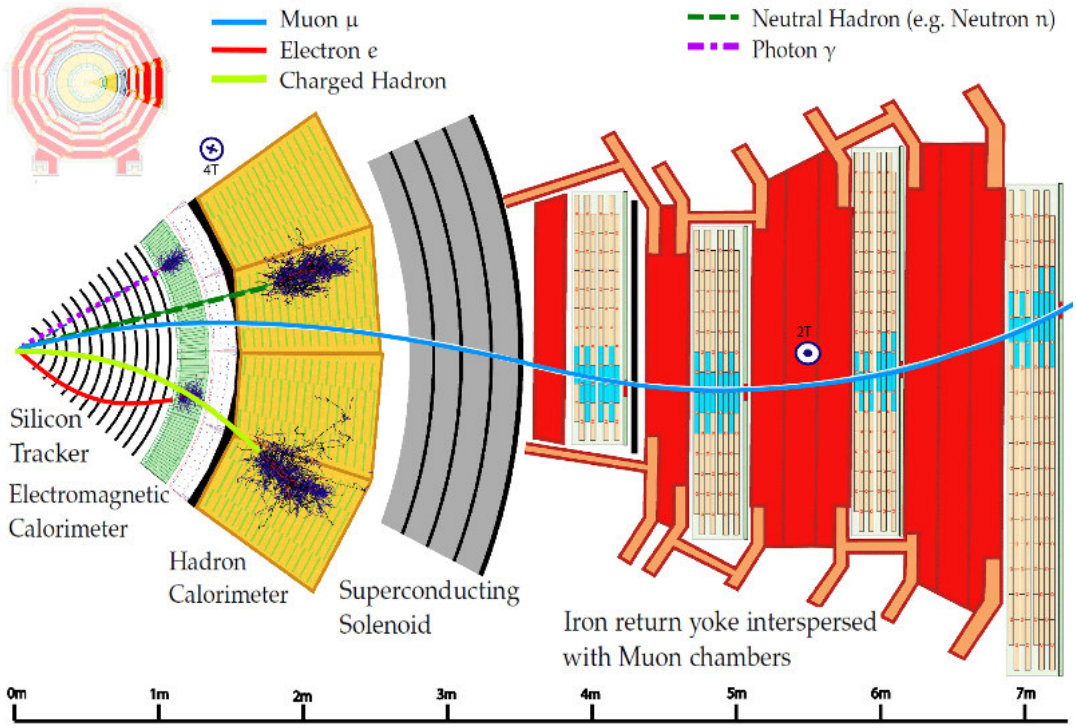

Figure 3: The CMS's detecor barrel in profile divided into five mayor sub detector systems with exemplary trajectories of different particles. Retrieved from [19].

Outgoing from the collision point in the center of the detector three layers of silicon-pixel-detectors, followed by ten layers of silicon-strip-detectors, record the trajectories of charged particles and reconstruct secondary vertices. The pixel detector is composed of 66 million silicon pixels with a sensitive area of 100 μm x 150 μm and a spatial resolution of 10 μm to 35 μm. They are necessary for a precise spatial resolution near the interaction point, but also to distinguish different trajectories from each other, as the particle rate near the interaction point is very high. The strip detector is made of silicon-strip-modules with a spatial resolution in range of 15 μm to 45 μm as a function of distance to the beam pipe. The overall track momentum resolution [20] of the tracker is combining both silicon detectors up to

$$\frac{\sigma_{p_T}}{p_T} = 0.15\% \cdot p_T[\mathrm{GeV}] \oplus 0.5\% \tag{4}$$

where $\oplus$ stands for the quadratic summation of the terms. The track momentum resolution has a plateau of 0.5% and decreases with increasing particle momentum.

The next sub detector is the electromagnetic calorimeter (ECAL), which is used to measure electromagnetic interacting particles like electrons. Electromagnetic interacting particles cause particle showers by a sequence of alternating bremsstrahlung radiation and pair production. In this way the energy of the initial electromagnetic interacting particle is divided into a high number of gammas and electron-positron pairs, which result from this interaction sequence. The energy of photons with wavelengths within the optical spectrum are measured by photodetectors. Since the particle's energy is proportional to the number of detected photons within the optical spectre, this sub detector is able to measure the energy of the electromagnetic interacting particle.
The ECAL is made of around 76000 scintillating $PbWO_4$ crystals of which around 61000 crystals are formed cylindrical around the barrel. They have a quadratic surface increasing from $(22 \text{ x } 22)\text{mm}^2$ next to the beam pipe to $(26 \text{ x } 26)\text{mm}^2$ furthest in the barrel. The endcaps contain around 7500 crystals each. Avalanche photo detectors measure scintillation light in the barrel, whereas vacuum photo detectors are used in the endcaps, due to higher radiation there. The energy resolution of the ECAL [21] has been determined using test beams to

$$\frac{\sigma_E}{E} = \frac{2.8\%}{\sqrt{E[GeV]}} \oplus \frac{12\%}{E[GeV]} \oplus 0.3\% \tag{5}$$

where the resolution is given by three terms: the stochastic (first), noise (second) and constant term (third). The resolution improves with increasing energy. For a high energy particle, such as an electron with an energy of 1 TeV, a plateau resolution of 0.3% is reached.

The energy loss through electromagnetic interaction of heavy, charged particles in matter is given by the Bethe Bloch formula [2] for hadrons with a momentum of up to some hundred GeV within the experiment. Here heavy refers to particles with much higher mass compared to the electron mass, which is applicable for hadrons, like for instance a charged pion with a rest mass of $m_{\pi^\pm} = 0.140$ GeV [2]. Since the energy loss of high energetic hadrons via electromagnetic interactions, described by the Bethe-Bloch formula, is negligibly small relative to their energy, hadronic particles pass the ECAL. They need to be detected in the hadronic calorimeter (HCAL). The HCAL is located around the ECAL and consists of 16 absorber layers of steel or brass alternating with scintillators, which are used to measure the energy loss of charged or uncharged hadronic particles. Because hadrons interact via strong force, they loose most of their energy via strong interactions due to the high mass density and thickness of the absorbent material. Test beams studies showed, that for the complete calorimetric system, pion energies can be reconstructed with a energy resolution [22] of

$$\frac{\sigma_E}{E} = \frac{115\%}{\sqrt{E[GeV]}} \oplus 5.5\% \tag{6}$$

The centerpiece of CMS is a superconducting solenoid magnet with a diameter of 6 m and which is cooled down to 4.7 K. The magnetic field in the silicon tracker, ECAL and HCAL is almost homogeneous with a field strength of 3.8 T, which allows to determine the transverse momentum of particles interacting by Lorenz force. A iron return yoke is used to shape the magnetic field on the outside of the calorimeters.

Since muons are minimal ionizing particles, they pass the mentioned calorimeters easily with only a little energy loss. 250 chambers with around 172000 drift tubes, 520 cathode strip chambers and 610 resistive plate chambers guarantee together with information of the silicon tracker an overall transverse momentum resolution of up to 5% for highly energetic muons around 1 TeV. Even though the signal of this analysis does not contain muons, a precise muon system is indispensable to identify muons, which can be misidentified as electrons or taus otherwise.

2.3 MEASUREMENT VARIABLES

By convention the coordinate origin is the nominal interaction point, the x-axis points towards the center of the LHC ring and the z-axis leads parallel to the beam axis. The **azimuthal angle** ϕ lies in the x-y-plane, measured from the x-axis, and the polar angle θ describes the angle to the beam axis. The **pseudorapidity** η is used since $\Delta\eta$ is invariant under Lorentz transformation and defined by

$$\eta = -\ln\left(\tan\left(\frac{\theta}{2}\right)\right) \tag{7}$$

Because of the magnetic field's orientation, the variable η is useful to describe physical variables transverse to the beam axis like the **transverse momentum** $p_T = |\vec{p}| \cdot \sin(\theta)$ or the **transverse energy** $E_T = E \cdot \sin(\theta)$.
Another Lorentz invariant quantity is the **invariant mass M**, given by

$$M = \sqrt{\left(\sum_i E_i\right)^2 + \left\|\sum_i \vec{p}_i\right\|^2} \tag{8}$$

whereby over all energies E_i and momenta $\vec{p}_i$ is summed. Using conservation of transverse momentum by summing the momentum of all particles of an event, one can define missing **transverse energy** $\vec{\not{E}}_T$

$$\vec{\not{E}}_T = -\sum_i \vec{p}_{T,i} \tag{9}$$

The sum is usually not zero, since often not all particles are detected and missing transverse momentum can be used to consider them. Using the pseudorapidity one can define the spatial distance between two objects (particles) by

$$\Delta R = \sqrt{(\Delta\phi)^2 + (\Delta\eta)^2} \tag{10}$$

2.4 EVENT RECONSTRUCTION

To reconstruct single particles and events with various sub detectors, generally the particle-flow algorithm (PF) [23] is used. First particles and than particle jets are reconstructed. Finally missing transverse energy $\not{E}_T$, caused for example through not detected neutrinos, is calculated.

2.4.1 *Tau Reconstruction*

Being the heaviest lepton with a mass of 1.78 GeV, taus have a very short life-time of $\tau \approx 29$ ps and a decay length of about $c \cdot \tau \approx 87$ µm [2]. They decay either leptonically into a $\mu^- \bar{\nu}_\mu \nu_\tau$ or $e^- \bar{\nu}_e \nu_\tau$ final state with an overall branching ratio (BR) of about 37% [9] or hadronically to a combination of charged and neutral mesons plus a neutrino. Leptonically decaying taus decay in an electron or a muon plus neutrino, which are strongly boosted in one direction at high energies. Due to the boost of the neutrino and the lepton in the same direction, no missing transverse energy is recognized. As a result only the lepton in final state is reconstructed but not the tau. At low energies the lepton and neutrino in final state are not strongly boosted, but their decay length is too short to reach the innermost pixel detector. Therefore only hadronically decaying taus are reconstructed as taus in CMS and considered in this analysis.

Nearly all hadronically decaying taus decay either into one charged pion plus neutrino or via ρ^- or a_1^- resonances into final state with one or three charged mesons. Table 5 summarizes the dominant hadronic decay modes. Most of the particles of the decay modes in final state

Table 5: Branching Ratio (BR) [9] of the dominant τ_h decays and mass of any intermediate resonance in natural units [24] . The h stands for both pion π and kaon K.

DECAY MODE	RESONANCE	MASS (MeV)	BR
$\tau^- \to h^- \nu_\tau$			11.6%
$\tau^- \to h^- \pi^0 \nu_\tau$	ρ^-	770	11.6%
$\tau^- \to h^- \pi^0 \pi^0 \nu_\tau$	a_1^-	1200	26.0%
$\tau^- \to h^- h^+ h^- \nu_\tau$	a_1^-	1200	9.5%
$\tau^- \to h^- h^+ h^- \pi^0 \nu_\tau$			9.8%

are pions. Charged pions ($\pi^\pm$) have a life-time of $\tau \approx 2.6 \cdot 10^{-8}$ s [9] and a decay length of about 7.8 m. Due to the long decay length, charged pions cause electromagnetic showers in the ECAL and HCAL. The curved trajectory is detected and the energy is measured in the HCAL, where the hadron is absorbed. Neutral pions (π^0) decay almost instantaneously (within $\tau \approx 8.4 \cdot 10^{-17}$ s) into a $\gamma\gamma$ pair [2]. Therefore, neutral pions cannot be measured directly, but they can be reconstructed by using special criteria for detected photos in the ECAL. The used algorithm for tau reconstruction is the "Hadron Plus Strips" (HPS) algorithm [25], which uses the CMS Particle Flow Algorithm [23]. The Particle Flow Algorithm is used here for the detection of photons and charged hadrons, which are used to reconstruct the hadronic tau decay modes.

The ECAL has an energy resolution σ_E/E of better than 0.5% for unconverted photons with $p_T > 100$ GeV [26]. Due to its' fine granularity, detected photons or electrons can be matched to a single tau decay channel and are denoted as a "strip". These clustering into strips proceeds iterative, whereby the electron, originating from pair production, or photon with high-

est p_T, which is not already assigned to a existing strip, initiates a new strip with an appointed window and position η and ϕ. The next highest p_T electron or photon passing the window is merged into the strip until no further particles are left within the window. The final strip position results from the energy-weighted average of all the strip's constituents. The size of the window $\Delta\eta$ x $\Delta\phi$ was fixed to 0.20 x 0.05 during run 1. In the new algorithm, which was adjusted for runs with $\sqrt{s} = 13$ TeV, the size is a function of the photon's or tau's p_T to enlarge the window for low p_T electrons from pair production, whose bending in the magnetic field increases with lower p_T [25].

The HPS reconstructs only the hadrons of the tau decay. These part is called the "visible" part of the hadronically decaying tau and is denoted as τ_h within this analysis. The neutrino or more precise the missing transverse energy of the decay mode is excluded within the τ_h. The decay modes of Table 5 are considered by the HPS algorithm as follows, where Figure 4 illustrates the algorithm in simplified terms.

- One charged hadron h^- is reconstructed corresponding to $h^-\nu_\tau$ (Figure 4a).
- One charged hadron h^- and a π^0 are reconstructed corresponding to $h^-\pi^0\nu_\tau$ decay mode, where the π^0 is reconstructed by photons in one single strip originating from the π^0 decay (Figure 4b). A neutral pion with not enough energy to pass the strip reconstruction criteria, will be not detected, but the tau can still be detected considered as a $h^-\nu_\tau$ decay mode.
- One charged hadron h^- and two π^0 are reconstructed to $h^-\pi^0\pi^0\nu_\tau$ decay mode, where the neutral pions correspond to two strips with two well separated photons.
- Three charged hadrons decay corresponding to the $h^-h^+h^-\pi^0\nu_\tau$ decay mode, where all three hadrons have to be reconstructed from the same secondary vertex.

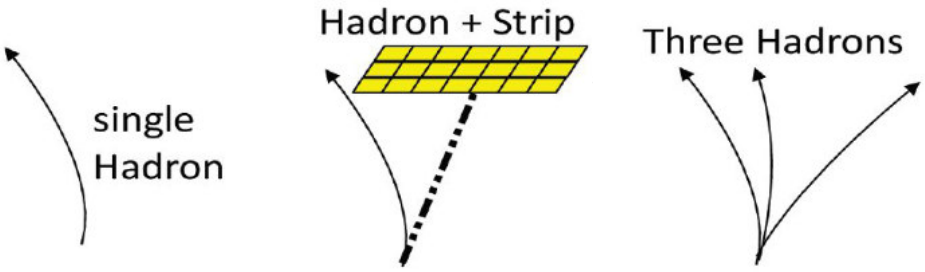

(a) Single hadron $h^\pm$ decay mode.

(b) Decay via resonance $\rho^\pm \to h^\pm\pi^0$.

(c) Decay via resonance $a_1^\pm$ into three hadrons. Mostly $\pi^+\pi^-\pi^+$, $\pi^-\pi^+\pi^-$ or $\pi^\pm\pi^0\pi^0$.

Figure 4: Illustration of different τ_h decay modes recognized by the HPS algorithm. Taken from [27].

2.4.2 *Electron Reconstruction*

Electrons are detected in the silicon tracker and ECAL through bremsstrahlung, emitting photons along the electron trajectory. Due to the orientation of the magnetic field, bremstrahlung is emitted only transverse in ϕ direction until the electron is absorbed in the ECAL.
Hadrons pass the ECAL into the HCAL, whereas electrons are absorbed in the ECAL before. Therefore trajectories of electrons must not have a entry in the HCAL. Since the bremsstrahlung energy loss distribution of electrons in matter is non-Gaussian, a special Gaussian sum filter (GSF) [28] algorithm is used for reconstruction of the electron's trajectory.

3 SIGNAL, BACKGROUND- AND DATA-SET

The object of search in this analysis is a resonance of a tau sneutrino $\tilde{\nu}_\tau$, decaying into an $e\tau$ pair. The underlying model treats the $\tilde{\nu}_\tau$ as the lightest supersymmetrical particle (LSP), which decays into a channel of SM particles, violating the lepton number. Information on R-parity and violation of lepton number can be found in Section 1.2.2. In this chapter the signal is described (Section 3.1), an overview of relevant background processes and their MC simulation is given (Section 3.2), as well as the data set (Section 3.3), used in this analysis.

3.1 SIGNAL

The Yukawa couplings λ and λ' of Equation 2 lead to lepton number L violation, whereas coupling λ'' in Equation 3 violates baryon number B. With reference to the superpotential W_{RPV}, which is the sum of W_{LNV} and W_{BNV}, the different couplings induce various free parameters. Irrelevant couplings are set to zero. Further assumption of baron triality [14] voids coupling λ'' and baryon number violation.
A simplified model with a minimum of three parameters is used in this analysis for the production of a RPV SUSY resonance, decaying into a tau and electron pair. Following aspects lead to the used RPV signal model

- The tau sneutrino $\tilde{\nu}_\tau$ is resonantly produced and assumed to be the candidate for the LSP and therefore only decays into SM particles.
- The tau sneutrino $\tilde{\nu}_\tau$ is produced in a quark-antiquark annihilation at a proton-proton collision. The production coupling therefore is λ'_{311}.
- The tau sneutrino $\tilde{\nu}_\tau$ decays with the coupling λ_{313} and λ_{331} into the $e\tau$ final state with a mass $M_{e\tau}$.
- A decay into other final states is possible as well, but not part of this analysis and therefore couplings into them are set to zero.

In this analysis the process $q\overline{q} \to \tilde{\nu}_\tau \to e\tau$ is researched (also see Feynman diagram Figure 5), whereby $\lambda'_{311} = 0.01$ and $\lambda_{313} = \lambda_{331} = 0.01$. All other couplings λ'_{ijk} and λ_{ijk} are set to zero.

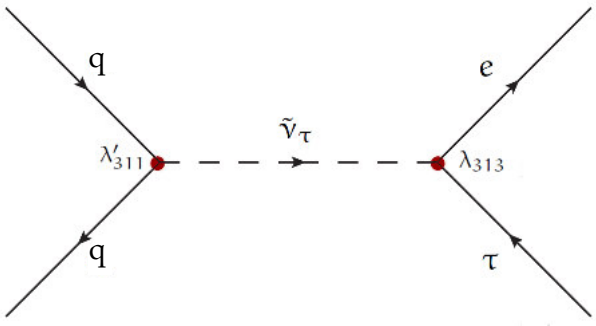

Figure 5: Resonant production of a $\tilde{\nu}_\tau$ in $q\overline{q}$ annihilation, decaying into a $e\tau$ pair. The coupling λ_{313} is according to the $e^-\tau^+$ final state. The final state of $e^+\tau^-$ is possible by the coupling λ_{331}, which is considered as well in this analysis.

3.2 BACKGROUND

To differentiate between potential new physics and SM processes, it is essential to use Monte Carlo simulations for the background expectation. In the following section the most important SM processes, divided into two fundamental categories, are illustrated. SM processes with a tau, which can decay hadronically, and electrons in the final state are classified as "prompt background", whereas processes that can be misidentified as a electron and tau, are classified as "fake background".

3.2.1 *Prompt Background*

Processes like *WW* (Figure 6a) , *WZ* (Figure 6b) or ZZ (Figure 6c) can decay into a $e\tau + X$ and are important background for an invariant mass $M_{e\tau}$ above 500 GeV. ZZ and *WZ* productions are less important than *WW* due to its smaller cross section times branching ratio. Single top (Figure 6d) or $t\bar{t}$ (Figure 6e) productions can decay into $e\tau$ channel as well and contain further b jets (which are possibly misidentified as hadronic taus). They are dominant for lower invariant $e\tau$ masses below 1 TeV.

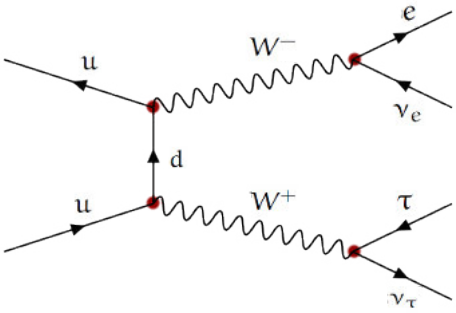

(a) *WW* to $e\nu_e\ \tau\nu_\tau$

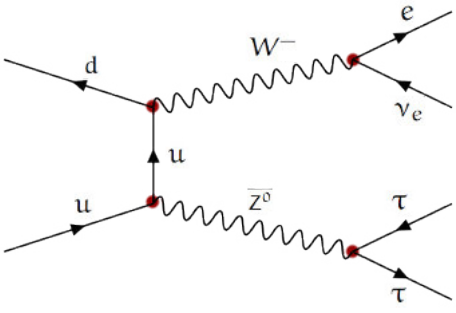

(b) *WZ* to $e\nu_e\ \tau\tau$

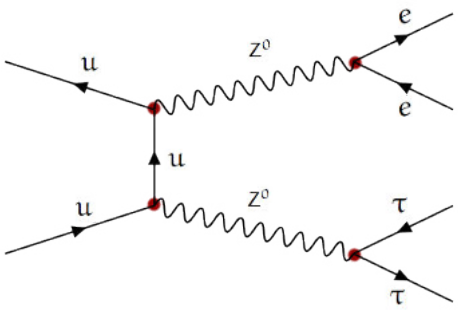

(c) ZZ to $ee\ \tau\tau$

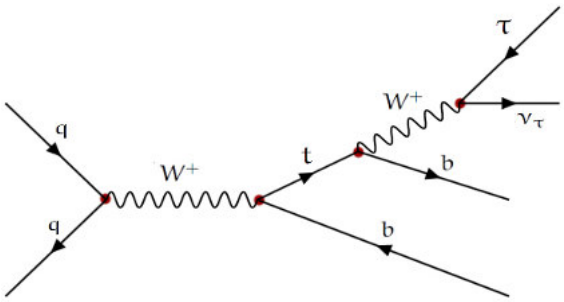

(d) Single Top production

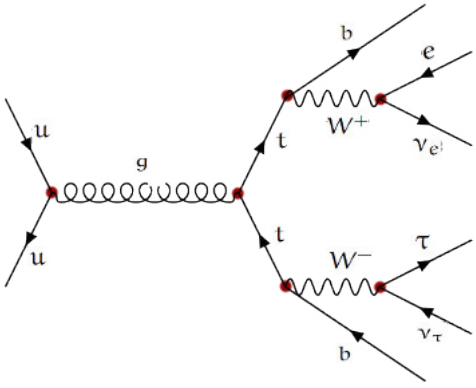

(e) $t\bar{t}$ production

Figure 6: Exemplary Feynman diagrams of "prompt background" processes in leading order.

3.2.2 *Fake Background*

Due to the reconstruction of taus in this analysis through the hadronic decay channel (see Section 2.4), hadronic jets of other SM processes can be misidentified as hadronically decaying taus. In addition an $e\tau$ final state can be reconstructed falsely by misidentified electrons or taus through other leptons.
The Drell-Yan process (Figure 7a) describes a hadronic scattering process, where a quark-antiquark annihilation with a connecting virtual photon or Z boson leads to a lepton-antilepton pair. Besides misidentify of an $e\bar{e}$ or $\mu\bar{\mu}$ pair, a single tau of a $\tau\bar{\tau}$ pair can decay into an electron plus neutrino producing prompt background. Another source of potentially misidentified leptons is the $W\gamma$ or $Z\gamma$ process (Figure 7b), where for example the W decays into a tau and the photon is either misidentified as an electron, or the photon converts into an electron. The jet background consists of events where a jet is misidentified as an electron or

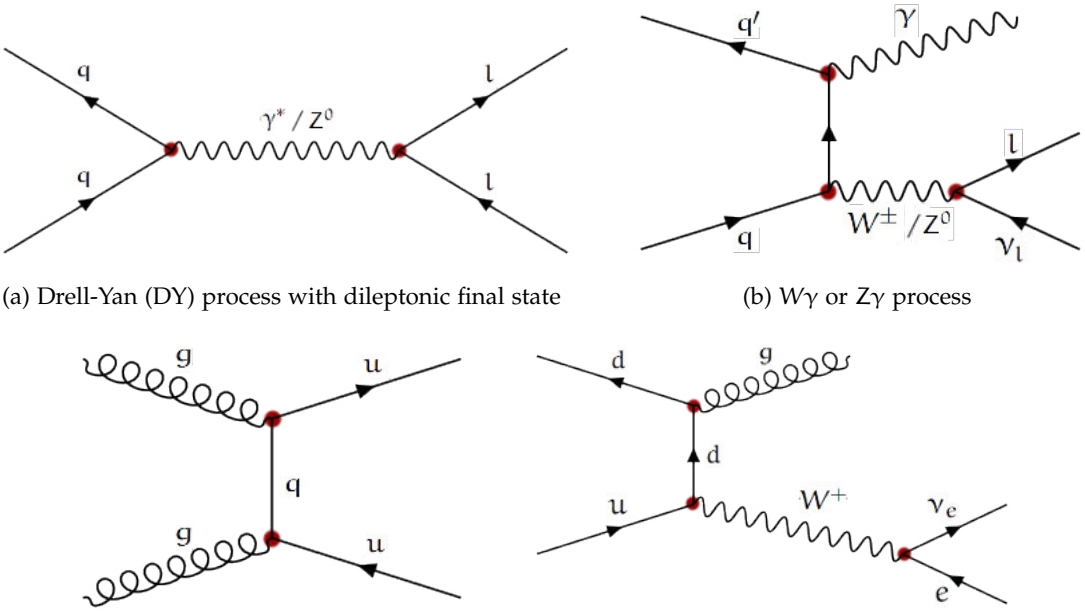

(a) Drell-Yan (DY) process with dileptonic final state

(b) $W\gamma$ or $Z\gamma$ process

(c) Exemplary QCD process

(d) W+Jets process with an electron in final state

Figure 7: Exemplary Feynman diagrams of "fake background" processes in leading order.

tau, that passes the selection. Multijet QCD processes are treated in this analysis, since they have a large cross section, that gives these processes a important role for background events. These background events come from quarks, generating boosted particle streams through self-coupling gluons. Figure 7c shows a possible QCD jet process exemplary. The W plus jet process (Figure 7d) can cause an electron (of the W decay) and a gloun to be misidentified as an electron plus τ_h pair.

3.3 DATASET

This analysis is based on data of the LHC with a integrated luminosity of $\mathcal{L}_{int} \approx 2.7$ fb^{-1} and a nominal center-of-mass energy of $\sqrt{s} = 13$ TeV recorded in the year 2015. Data sets, which contain a single electron trigger, are used, since a single electron is required in the final state of the RPV signal. For details see Table 6. To compare the Monte Carlo samples of

Table 6: Used Dataset from CMS. A systematic uncertainty of 2.7% is assigned to the integrated luminosity and is used for background rates.

DATASET	RUN RANGE	$\mathcal{L}_{int}$ (fb^{-1})
DataRun2015D/16Dec2015/SingleElectron	251027-260627	2.671 ± 0.072

background processes and the signal with the data, it is required to reweight the MC samples to the luminosity of the data by multiplying a certain weight factor. The weight factor is given by multiplying the sample's cross section σ_s with the integrated luminosity $\mathcal{L}_{int}$ divided by the absolute event number $N_{E\nu}$ of the sample

$$w = \frac{\sigma_s \cdot \mathcal{L}_{int}}{N_{E\nu}} \tag{11}$$

3.4 MONTE CARLO SAMPLES

3.4.1 *RPV signal Monte Carlo Simulation*

The RPV signal Monte Carlo samples have been produced with the CalcHEP generator [29] combined with with Pythia 8 [30] for parton showering and hadronisation. The generated events are processed through a full simulation of the CMS detector based on GEANT 4 [31]. The cross section for the signals is calculated in leading order (LO) QCD and scaled with k-factors to next-to-leading order (NLO) QCD. Table 12 contains the information about the binning, cross section, number of generated events and information to the Monte Carlo generator for each signal process. The table can be found in the appendix.

3.4.2 *Background Monte Carlo Simulation*

The complete background for this analysis is based on Monte Carlo simulation. Table 13 contains information about the binning, cross section, number of generated events and information to the Monte Carlo generator for each background process. The generated events are processed through a full simulation of the CMS detector based on GEANT 4 [31]. Background processes which contain two bosons ($W^{\pm}$ and Z^0) are summarized and denoted as Diboson-background in the analysis. The table can be found in the appendix.

Due to inadequate Monte Carlo simulations of QCD processes, a disagreement between QCD background and the data at some ranges of energy scale occurs in this analysis. Additionally, the insufficient amount of statistics for QCD processes causes high uncertainties in the $e\tau$ invariant mass distribution. Since the time required to perform a QCD analysis based on the used data exceeds the time scale of this analysis, electron enriched QCD Monte Carlo simulations are used.

4 ANALYSIS

In the first part of the analysis, selection criteria for events of the RPV signal are discussed. Furthermore cuts on kinematic variables are optimized and applied, to reach a separation between background and signal. Finally a limit on the cross section times branching ratio for the production of a $\tilde{\nu}_\tau$ and decay into a $e\tau$ pair is calculated.

4.1 ELECTRON SELECTION

4.1.1 *Trigger*

Due to the RPV signal with an electron and tau in the final state, the single-electron High-Level Trigger (HLT) "HLT_Ele105_CaloIdVT_GsfTrkIdT" with the lowest E_T threshold of the unisolated single electron was chosen [32]. The trigger requires a single electron with following conditions [33]

- Transverse energy of the electron must be at least $E_T^{ele} > 105$ GeV (Ele105).
- Ratio between the deposited HCAL energy H in a cone of $\Delta R < 0.14$ around the electron's position in the ECAL and the deposited energy E in the Super Cluster (Section 2.2) must be $H/E < 0.15$.
- An electron must pass the ECAL identification discriminator "Very Tight" (CaloIdVT) with cluster shape $\sigma_{i\eta i\eta} < 0.012$ (barrel) and $\sigma_{i\eta i\eta} < 0.032$ (endcap). The variable $\sigma_{i\eta i\eta}$ is a measure of the electron's energy spread in a 5 x 5 ECAL crystal block (Section 2.2) placed around the initially seeded crystal in units of η.
- ECAL entry plus angular matching between Super Cluster and electron track (GsfTrkIdT) with $\Delta\eta < 0.008$, $\Delta\phi < 0.1$ (barrel) or $\Delta\eta < 0.011$, $\Delta\phi < 0.1$ (endcap).

4.1.2 *Selection with HEEP ID Cuts*

For data and Monte Carlo, high E_T electrons are selected with dedicated cuts of the HEEP ID V6.1 [34]. Table 7 lists the used cuts for electron selection divided into barrel and endcap.

Table 7: Used High Energy Electron Positron (HEEP) ID V6.1 cuts [34]. Not defined variables are explained on the next page.

VARIABLE	BARREL	ENDCAP
E_T	> 35 GeV	> 35 GeV
η range	$\lvert\eta_{SC}\rvert < 1.4442$	$1.566 < \lvert\eta_{SC}\rvert < 2.5$
is ECAL driven	✓	✓
$\lvert\eta_{in}\rvert$	< 0.004	< 0.006
$\lvert\Delta\phi_{in}\rvert$	< 0.06	< 0.06
H/E	$< 1/E + 0.05$	$< 5/E + 0.05$
full 5 x 5$\sigma_{i\eta i\eta}$	-	< 0.03
full 5 x 5E^{2x5}/E^{5x5}	> 0.94 or $E^{1x5}/E^{5x5} > 0.83$	-
EM + Had Depth 1 Isolation	$< 2 + 0.03 \cdot E_T + 0.28 \cdot \rho$	$< 2.5 + 0.28 \cdot \rho$ for $E_T < 50$ GeV else $< 2.5 + 0.03 \cdot (E_T - 50) + 0.28 \cdot \rho$
Track Isolation: Track p_T	< 5 for $E_T < 95$ GeV else $< 5 + 1.5 \cdot \rho$	< 5 for $E_T < 100$ GeV else $< 5 + 0.5 \cdot \rho$
Inner Layer Lost Hits	$\leqslant 1$	$\leqslant 1$
$\lvert d_{xy}\rvert$	< 0.02	< 0.05

These cuts ensure, that electron tracks are isolated against tracks of particles, which cause an electron misidentification. Not defined variables of Table 7 are

- "ECAL driven" requires a particle track in the ECAL to reconstruct the electron with GSF algorithm [28].
- $|\eta_{in}|$ and $|\Delta\phi_{in}|$ describe the angular differences between the track direction, measured at the tracker's innermost layer, extrapolated to the primary vertex and measured position in the ECAL Super Cluster. The matching of these two tracks ensures the belonging to the same particle.
- $|\eta_{SC}|$ is the pseudorapidity of the electron's Super Cluster.
- $E^{n\times5}/E^{5\times5}$ describes the fraction of deposited energy in n x 5 crystals to the energy, deposited entire 5 x 5 cluster of the ECAL. In contrast to jets, electrons deposit their energy mostly in only up to two crystals.
- Track Isolation sums the p_T of all tracks in a area of $0.015 < \Delta R < 0.2$.
- EM + Had Depth 1 Isolation sums the transverse energy in a cone around the electron track in the ECAL and HCAL.

4.2 TAU SELECTION

The used algorithm for tau identification (ID) is the HPS algorithm (see Section 4.2). This algorithm uses particles, which were reconstructed in the detector, and calculates various values of these particles like for example their distance to other particles around a certain sphere. Subsequently these values are compared to requirements. The requirements are determined by a so called discriminator, which summarizes different required values to select particles with certain properties. Here, discriminators are considered, which select taus within a event. Since there are various different discriminators [35] to choose for tau selection, it is necessary to analyze different ones and choose an ID combination for isolation against particles, which can lead to tau misidentification. Here two quantities are used: The discriminator efficiency and the discriminator misidentification rate. Principally the discriminator efficiency gives the probability that a tau passes the discriminator and the discriminator misidentification rate gives the probability that a certain particle passes the discriminator and is therefore missidentified as a tau. The aim is to find the best compromise between the efficiency and misidentification rate.

In the first step of the tau ID, particles are required to fulfill $|\eta| < 2.3$, due to the maximal geometric acceptance of the detector [25], and a lower bound of transverse particle momentum of $p_T > 20$ GeV. The p_T bound is required by the HPS algorithm [35]. The HPS algorithm requires a specific combination of detected charged hadrons plus photons, which were reconstructed with strips in the ECAL, to reconstruct a tau. Since other particles like hadronic jets fulfill these requirements very often as well, they are misidentified as taus frequently.

Therefore, an algorithm called "decayModeFinding" is implemented in the first step of the tau selection within this analysis to reject misidentified jets by using the invariant mass of the reconstructed τ_h. Using the decay modes of Table 5 in Section 2.4.1, the invariant mass of the τ_h has to be next to the mass of the decays resonances ρ^- or a_1^- for the corresponding τ_h decay mode. The invariant mass of jets is evenly distributed and therefore a part of jets, which were misidentified as taus, are rejected.

4.2.1 *Isolation Discriminator*

Using the "decayModeFinding" discriminator is not sufficient enough to reject jets , which were misidentified as taus. Hadronic jets have a high multiplicity of particles, which is increasing with the energy of the jet. Objects of an τ_h, originating of an $\tilde{\nu}_\tau$ decay, should not contain further hadrons in the close proximity. Therefore, an additional discriminator is used, which requires special isolation criteria in a cone around the τ_h.
In high luminosity colliders like the LHC, single colliding bunches produce several separate collisions, so called pile-up. Neutral particles as π^0 and γ originating from pile-up may have entered the cone around a tau. As they cannot be rejected by tracking information, they may have mistakenly been included in the reconstruction. The isolation discriminators can be used to reject hadrons of pile-up.

Basically two different types of isolation discriminators are provided for tau reconstruction. These single types can be chosen with different threshold values.

In this section an isolation discriminator is selected due to the analysis of the discriminator's efficiency ϵ (Equation 12) and the related misidentification rate f_R (Equation 13). The efficiency is derived from the Monte Carlo simulation of the RPV signal (Section 3.4.1) and the misidentification rate from Monte Carlo simulations of the QCD processes and the $W + Jets \rightarrow l\nu$ samples (Section 3.4.2), which contain a great number of hadronic jets.

Since particles must fulfill the thresholds of $p_T > 20\ GeV$ and $|\eta| < 2.3$, generated as well as reconstructed particles, which do not fulfill these boundaries, are rejected for the calculation of the efficiency and the misidentification rate.

The **isolation discriminator efficiency** is calculated as follows.

For every generated tau, which decays hadronically, it is searched for a reconstructed particle, which passes the "decayModeFinding" discriminator in a cone of $\Delta R < 0.3$ around the position of the generated tau. The reconstructed particle, which fulfills both requirements and has the shortest distance ΔR to the generated tau, is considered as a correctly reconstructed tau.
These particles are used to calculate the fraction of the number of correctly reconstructed taus, which fulfill additionally the isolation discriminator (named "IsoDisc" in the argument), to the number of all correctly reconstructed taus.

$$\epsilon(p_T^{\tau,gen}) = \frac{N(p_T^{reco} > 20\ \text{GeV}\ \&\ |\eta^{reco}| < 2.3\ \&\ \text{DecayMode}\ \&\ \tau\text{-IsoDisc})}{N(p_T^{reco} > 20\ \text{GeV}\ \&\ |\eta^{reco}| < 2.3\ \&\ \text{DecayMode})} \tag{12}$$

The **isolation discriminator misidentification rate** is calculated as follows.

For every generated jet, it is searched for a reconstructed particle, which passes the "decayModeFinding" discriminator in a cone of $\Delta R < 0.3$ around the position of the generated jet. The reconstructed particle, which fulfills both requirements and has the shortest distance ΔR to the generated jet, is considered as a jet, which fulfills the "decayModeFinding" discriminator and is therefore misidentified as a tau.
These jets are used to calculate the fraction of the number of jets, which are misidentified as

taus and additionally fulfill the isolation discriminator (named "IsoDisc" in the argument), to the number of all jets, which are misidentified as a tau.

$$f_R(p_T^{jet,gen}) = \frac{N(p_T^{reco} > 20\ \text{GeV}\ \&\ |\eta^{reco}| < 2.3\ \&\ \text{DecayMode}\ \&\ \tau\text{-IsoDisc})}{N(p_T^{reco} > 20\ \text{GeV}\ \&\ |\eta^{reco}| < 2.3\ \&\ \text{DecayMode})} \tag{13}$$

Figure 9a and Figure 10a show the isolation efficiencies ϵ as a function of the generated tau's transverse momentum and Figure 9b and Figure 10b show the respective misidentification rates as a function of the generated jet's transverse momentum for a cut-based and a MVA-based isolation discriminator. Both types of discriminator are explained below the figures.

To compare the different cut- and MVA-based discriminators and estimate a good compromise between sufficient efficiency and low misidentification rate, the efficiency of the discriminators is plotted against the misidentification rate in Figure 8.

The misidentification rate of cut-based discriminators varies little, whereas the efficiency varies in steps of about 10% per working point with best efficiency of around 81% for p_T^τ above 1 TeV. Efficiencies of MVA-based discriminators increase almost gradually and are approximately independent from the $e\tau$ mass. Corresponding misidentification rates vary from 10^{-5} to 10^{-4}.

Since the efficiency varies strong relative to the misidentification rate with the working point, the discriminator with the highest efficiency above 90%, the MVA-based discriminator "byVLooseIsolationMVArun2v1DBoldDMwLT", is chosen in this analysis.

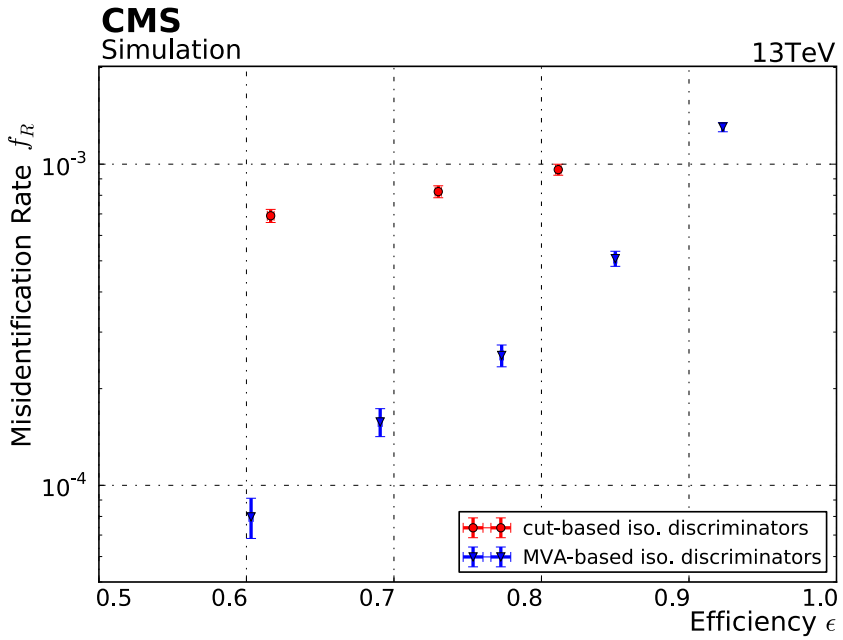

Figure 8: Efficiency ϵ against misidentification rate f_R of cut-based and MVA-based discriminators for different working points.

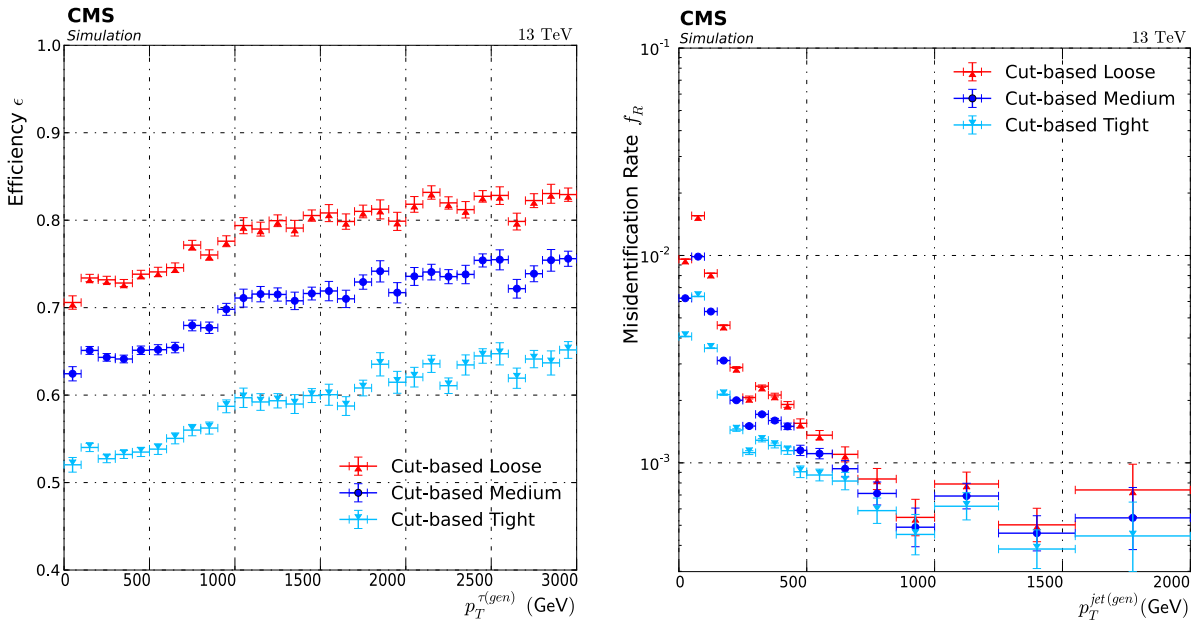

(a) Efficiency ϵ of cut-based discriminators.

(b) Misidentification Rate f_R of cut-based discriminators.

Figure 9: Efficiency and misidentification rate of cut-based isolation discrimnators. Information to the different working points is given in Table 8.

The **Cut-based** discriminator [25] selects charged particles of $p_T > 0.5$ GeV and photons of $E_T > 0.5$ GeV, which are reconstructed by the particle flow algorithm (PF) [23], within a cone around the τ_h of size $\Delta R = 0.3$.
Hadronically decaying taus passing the cut-based discriminator, need to fulfill the threshold value I_τ, which is the sum of transverse momenta of photons and charged particles:

$$I_\tau = \sum p_T^{charged}(d_z < 0.2 \text{ cm}) + \max(0, \sum p_T^\gamma - \Delta\beta) \tag{14}$$

where

- Cut values are: $I_\tau < 0.8$ GeV (tight), $I_\tau < 1.5$ GeV (medium), $I_\tau < 2.5$ GeV (loose).
- Tracks of charged particles are required to have a distance lower than 2 cm in z-direction to the τ_h's production vertex
- The effect of mismatched γs is reduced by the Delta Beta Correction $\Delta\beta = 0.2$ [25].
- Jets being misidentified as τ_h are vetoed by an additional threshold. The sum of deposited p_T of electrons or photons, detected in strips, which were used to reconstruct the τ_h, needs to fulfill

$$\sum p_T^{e/\gamma} < 0.1 \cdot p_T^\tau \tag{15}$$

- Charged particles are excluded, if photons were detected in the same strip.

Table 8 lists three different cut-based discriminators with their efficiencies and misidentification rates. The misidentification rates are approximated as constant on a plateau for $p_T^{jet,gen}$ above 500 GeV and the efficiencies are approximated as constant for $p_T^{\tau,gen}$ above 1 TeV.

Table 8: Analyzed cut-based discriminators with constant approximated efficiencies ϵ and misidentification rates f_R. The uncertainties are statistical and result from the approximation.

DISCRIMINATOR NAME	EFFICIENCY ϵ	MISSID. RATE f_R
by**Loose**CombinedIsolationDeltaBetaCorr3Hits	0.811 ± 0.002	$(96.2 \pm 3.8) \cdot 10^{-5}$
by**Medium**CombinedIsolationDeltaBetaCorr3Hits	0.730 ± 0.002	$(82.1 \pm 3.5) \cdot 10^{-5}$
by**Tight**CombinedIsolationDeltaBetaCorr3Hits	0.616 ± 0.002	$(69.0 \pm 3.2) \cdot 10^{-5}$

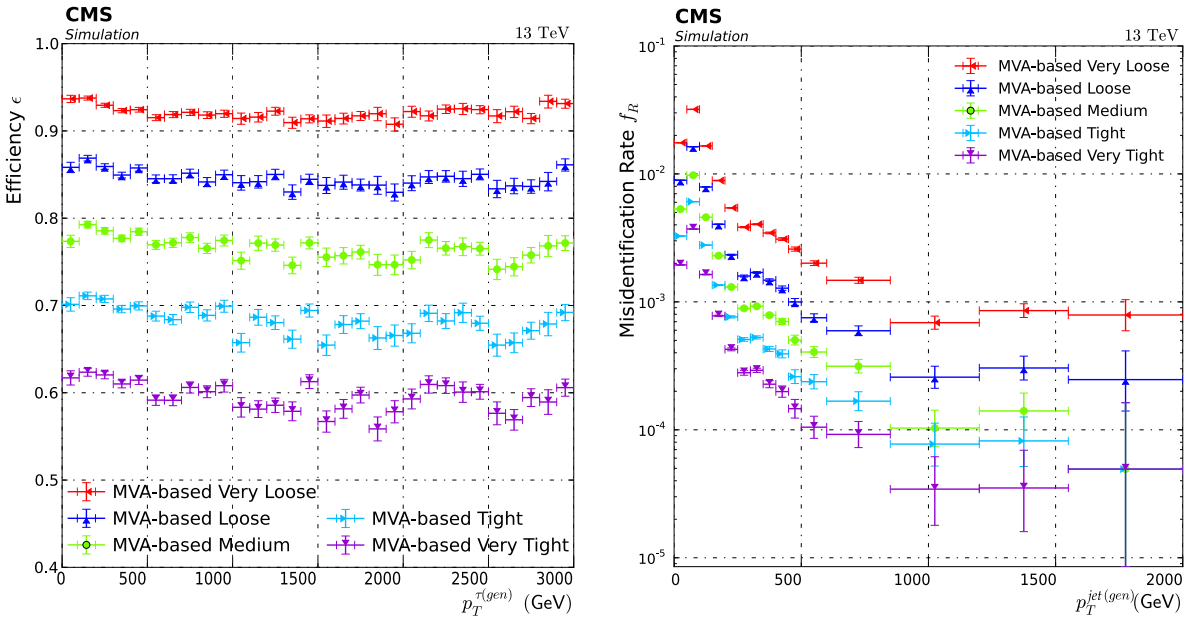

(a) Efficiency ϵ of MVA-based discriminators.

(b) Misidentification rate f_R of MVA-based discriminators.

Figure 10: Efficiency and misidentification rate of MVA-based isolation discriminators. Information to the different working points is given in Table 9.

Alternatively a **MVA-based** discriminator [25] can be chosen. The multivariate analysis (MVA) based isolation discriminator uses additionally the life-time of the τ to separate between τ_h candidates and hadron jets, misidentified as τ_h. Extending the cut-based discriminator, the MVA-based discriminator uses p_T^τ weighted quantities and information for calculating the cut values. Additional τ life-time and flight distance are considered to construct a secondary vertex for the tau.

The MVA-based discriminators are provided with five different working points, gradually increasing in τ_h reconstruction efficiency. A gradually increase of efficiency is also recognizable in Figure 10a from "Very Loose" to "Very Tight". Table 9 lists the different discriminators with their constant approximated efficiencies and misidentification rates. The misidentification rates were approximated for p_T^τ above 500 GeV and the efficiencies on the whole p_T^τ range.

Table 9: Analyzed MVA-based discriminators with constant approximated efficiencies ϵ and misidentification rates f_R. The uncertainties are statistical and result from the approximation.

DISCRIMINATOR NAME	EFFICIENCY ϵ	MISSID. RATE f_R
by**VLoose**IsolationMVArun2v1DBoldDMwLT	0.923 ± 0.001	$(130.5 \pm 4.3) \cdot 10^{-5}$
by**Loose**IsolationMVArun2v1DBoldDMwLT	0.850 ± 0.001	$(50.8 \pm 2.7) \cdot 10^{-5}$
by**Medium**IsolationMVArun2v1DBoldDMwLT	0.773 ± 0.001	$(25.4 \pm 2.0) \cdot 10^{-5}$
by**Tight**IsolationMVArun2v1DBoldDMwLT	0.691 ± 0.001	$(15.8 \pm 1.7) \cdot 10^{-5}$
by**VTight**IsolationMVArun2v1DBoldDMwLT	0.603 ± 0.001	$(8.0 \pm 1.1) \cdot 10^{-5}$

4.2.2 *Against Electron and Muon Discriminator*

Since high energetic electrons radiate bremstrahlung photons, electrons have a non negligible chance of being misidentified as charged pions or kaons. Especially isolated electrons, originating from Z- or *W*-boson decay, have a high probability of passing the tau ID. Since the signal does not contain muons, reconstructed $e\tau$ events, which include a muon next to the vertex, are rejected.

To reduce electrons or muons, which are misidentified as taus, additional against-electron and against-muon discriminators are analyzed and their effect is evaluated due to their efficiency and misidentification rate. The against-electron discriminators are based on a multivariate analysis algorithm for separating electrons from hadronic tau decays [25]. Variables of the ECAL and HCAL, which discriminate between electromagnetic and hadronic showers, in combination with photon-related variables are used as inputs of this algorithm. Especially the emission of bremsstrahlung radiation along the leading track of hadronically decaying taus is evaluated to separate electrons from τ_h decays. The against-muon discriminator vetoes particles, which have an entry in the muon calorimeter and a track within a certain cone of a reconstructed $e\tau$ pair.

The efficiency ϵ is derived from the Monte Carlo simulation of the RPV signal (Section 3.4.1) and the misidentification rate f_R from Monte Carlo simulations of the $Z \to ee$ processes for anti-electron discriminator and $Z \to \mu\mu$ processes for the anti-muon discriminator (Section 3.4.2)
The **against electron/muon discriminator efficiency** is calculated analogously to the isolation discriminator efficiency (Equation 12), whereas correctly identified taus additionally must pass the MVA-based "byVLooseIsolationMVArun2v1DBoldDMwLT" isolation discriminator. Here, these particles are used to calculate the fraction of the number of correctly reconstructed taus, which fulfill additionally the against-electron or muon discriminator (named "e/μ Disc" in the argument), to the number of all correctly reconstructed taus.

$$\epsilon(p_T^{\tau,gen}) = \frac{N(p_T^{reco} > 20\ \text{GeV}\ \&\ |\eta^{reco}| < 2.3\ \&\ \text{DecayMode}\ \&\ \tau\text{-IsoDisc}\ \&\ e/\mu\ \text{Disc})}{N(p_T^{reco} > 20\ \text{GeV}\ \&\ |\eta^{reco}| < 2.3\ \&\ \text{DecayMode}\ \&\ \tau\text{-IsoDisc})} \quad (16)$$

The **against electron/muon discriminator misidentification rate** is calculated analogously to the isolation discriminator misidentification rate (Equation 13), whereas electrons or muons are used instead of jets. The electrons or muons, which are misidentified as taus, furthermore must pass the MVA-based "byVLooseIsolationMVArun2v1DBoldDMwLT" isolation discriminator.
Here these particles are used to calculate the fraction of the number of electrons/muons, which are misidentified as taus and additionally fulfill the against-electron or muon discriminator (named "e/μ Disc" in the argument), to the number of all electrons/muons, which are misidentified as a tau.

$$f_R(p_T^{e\mu,gen}) = \frac{N(p_T^{reco} > 20\ \text{GeV}\ \&\ |\eta^{reco}| < 2.3\ \&\ \text{DecayMode}\ \&\ \tau\text{ -IsoDisc}\ \&\ e/\mu\ \text{Disc})}{N(p_T^{reco} > 20\ \text{GeV}\ \&\ |\eta^{reco}| < 2.3\ \&\ \text{DecayMode}\ \&\ \tau\text{-IsoDisc})} \quad (17)$$

Figure 11a and Figure 11c show the efficiencies ϵ of the against-electron/muon discriminator as a function of the generated tau's transverse momentum and Figure 11b and Figure 11d show the respective misidentification rates f_R as a function of the generated lepton's transverse momentum for discriminators of different working points. Table 10 lists the different discriminators with their constant approximated efficiencies and misidentification rates. To

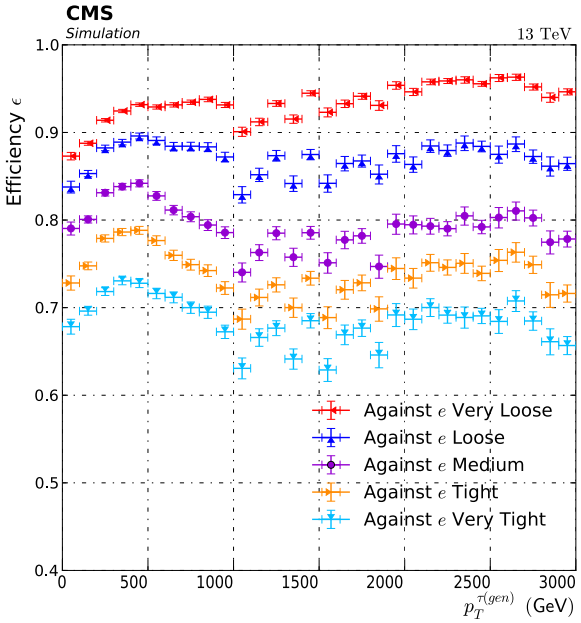

(a) Efficiency ϵ of against-electron discriminators.

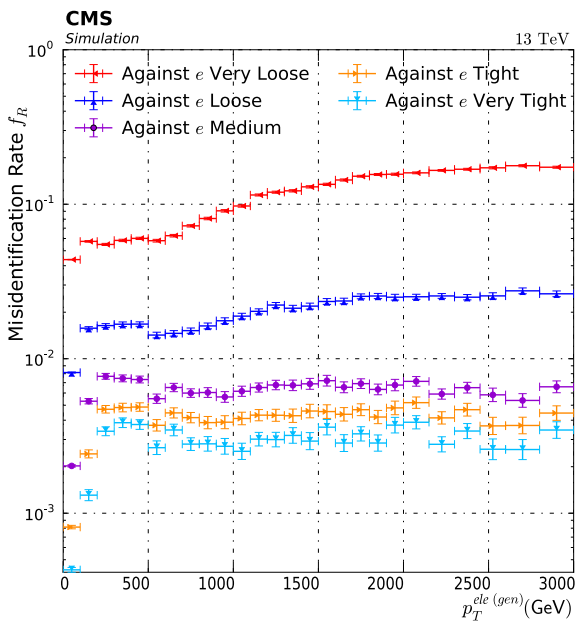

(b) Misidentification rate f_R of against-electron discriminators.

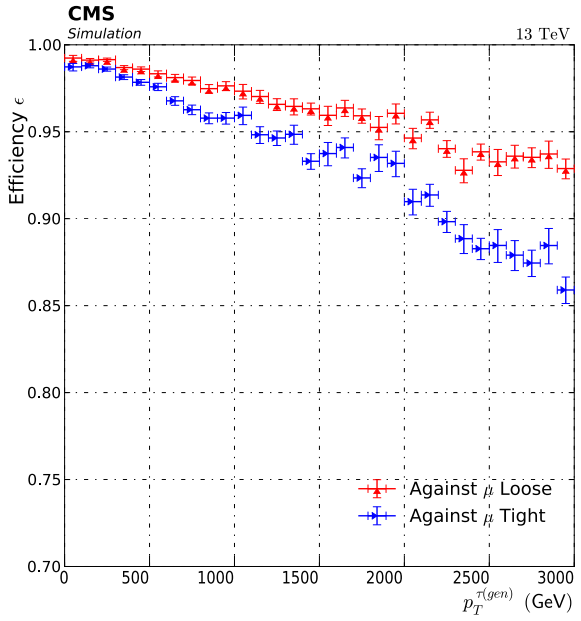

(c) Efficiency ϵ of against-muon discriminators.

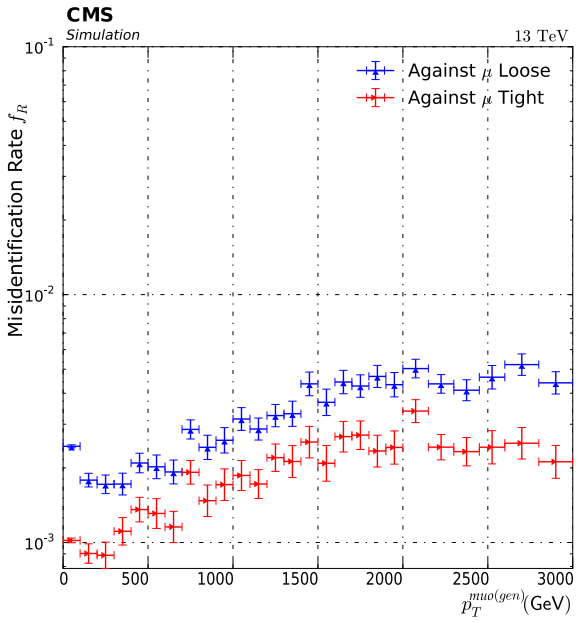

(d) Misidentification rate f_R of against-muon discriminators.

Figure 11: Efficiency and misidentification rate of against-electron and against muon discrimnators. Information to the different working points is given in Table 10.

compare the different against-electron and against-muon discriminators and estimate a good compromise between sufficient efficiency and low misidentification rate, the efficiency of the discriminators is plotted against the misidentification rate in Figure 12.

Table 10: Analyzed against-electron and against-muon discriminators with constant approximated efficiencies ϵ and misidentification rates f_R. The uncertainties are statistical and result from the approximation. The misidentification rates and the efficiencies of against-electron and against-muon discriminators were approximated for p_T^τ above 500 GeV.

DISCRIMINATOR NAME	EFFICIENCY ϵ	MISSID. RATE f_R
againstElectron**VLoose**MVA6	0.941 ± 0.001	$(110.0 \pm 0.2) \cdot 10^{-3}$
againstElectron**Loose**MVA6	0.875 ± 0.001	$(20.3 \pm 0.2) \cdot 10^{-3}$
againstElectron**Medium**MVA6	0.793 ± 0.002	$(6.3 \pm 0.1) \cdot 10^{-3}$
againstElectron**Tight**MVA6	0.740 ± 0.002	$(4.4 \pm 0.1) \cdot 10^{-3}$
againstElectron**VTight**MVA6	0.689 ± 0.002	$(3.0 \pm 0.1) \cdot 10^{-3}$
againstMuon**Loose**3	0.968 ± 0.001	$(3.3 \pm 0.1) \cdot 10^{-3}$
againstMuon**Tight**3	0.947 ± 0.001	$(2.0 \pm 0.1) \cdot 10^{-3}$

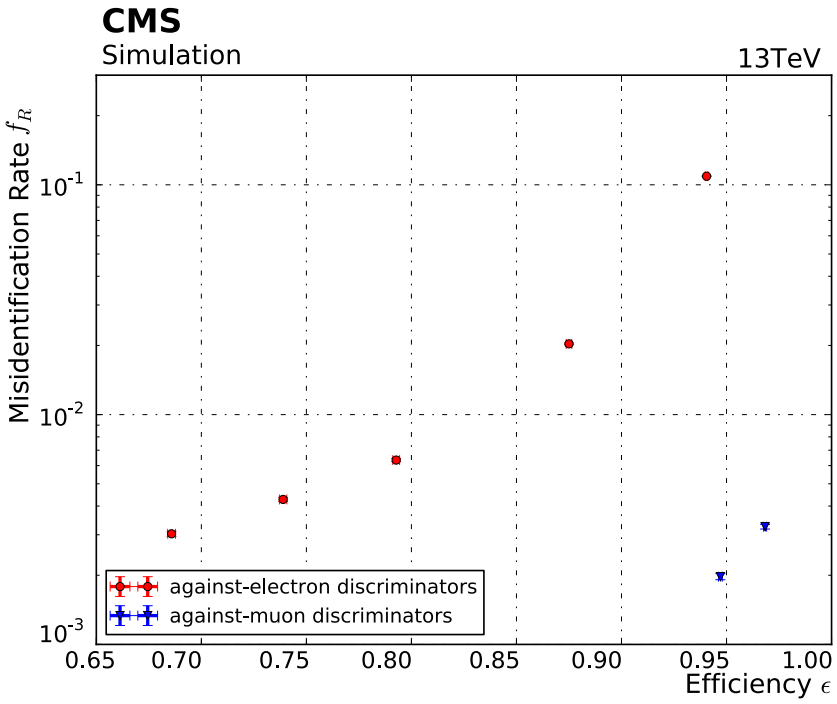

Figure 12: Efficiency ϵ against the misidentification rate f_R of against-electron and against-muon discrimnators. Information to the different working points is given in Table 9 and Table 10.

Because the misidentification rate of the against-electron discriminator with the best efficiency (very loose working point) is too high, the "againstElectronLooseMVA6" discriminator is chosen. The against-muon discriminators efficiencies decrease with increasing $p_T^{\tau(gen)}$, where the "againstMuonTight3" discriminator's efficiency decreases much stronger (with about 3% per TeV more) than the "againstMuonLoose3" discriminator. Since the misidentification rate of both discriminators have the same order, the "againstMuonLoose3" discriminator is chosen in this analysis.

4.3 EVENT SELECTION

In this section, the reconstruction of the invariant $e\tau$ mass is described. Further event selection criteria are introduced to reduce the SM background events to a minimum.

The decay of a tau sneutrino into an $e\tau$ pair contains an electron, a certain number of hadrons corresponding to the hadronic decay mode of the tau and a neutrino in final state. Therefore an event is required to have one electron, a τ_h and at least 30 GeV of missing transverse energy to be selected. As only the absolute value and the azimuthal angle ϕ of the missing transverse energy is determinable, it is necessary to use an assumption to reconstruct the momentum of the neutrino.
Since the rest mass of the tau sneutrino must be much higher compared to rest masses of SM particles, the tau and the electron have high momentum compared to their rest mass after the decay of the $\tilde{\nu}_\tau$. The hadrons and the neutrino of the hadronically decaying tau are therefore boosted in the same direction. Thus the η of the τ_h is assumed to be the same for the neutrino, to reconstruct the neutrino's momentum. The invariant $e\tau$ mass is given through

$$M_{e\tau} = \sqrt{(p_{\tau_h} + p_e + \not{E})^2} \tag{18}$$

Here p_{τ_h} is the four-momentum of the hadrons, originating from the hadronically decaying tau and p_e is the four-momentum of the electron. $\not{E}$ denotes the four-momentum of the neutrino, reconstructed with missing transverse energy $\not{E}_T$ and the assumption of η.

In the next part of this analysis, five cuts on background, signal and data are applied, where the cut values of two cuts are given by theoretical consideration, whereas the cut values of the remaining three cuts are kinematic and need to be optimized. The number of signal events should be as constant as possible.

The specific kinematic cut value is optimized by calculating expected upper limits on the cross section times branching ratio. All the background processes were used for the limit calculation and three exemplary RPV signals at a resonant $e\tau$ mass of 300 GeV , 1600 GeV and 3500 GeV. Due to the cut values, the variation of the cross section times branching ratio limit with the applied cut values is decreasing rapidly for increasing τ-sneutrino invariant mass. The best cut value will be chosen according to the best resulting limit, which is the one with the lowest cross section times branching ratio. The range of analyzed cut values is selected due to the theoretical motivation of the kinematic cut.

Figure 13 shows the invariant mass distribution of the $e\tau$ final state in preselection state. This state means, that no cut applied. Only the electron and tau selection criteria of Section 4.1 and Section 4.2 as well as the trigger were used to select the events. The exemplary shown signal (red line) shows a RPV resonance of invariant $e\tau$ mass of 800 GeV. Beneath the mass distribution a ratio of data to Monte Carlo events is given.

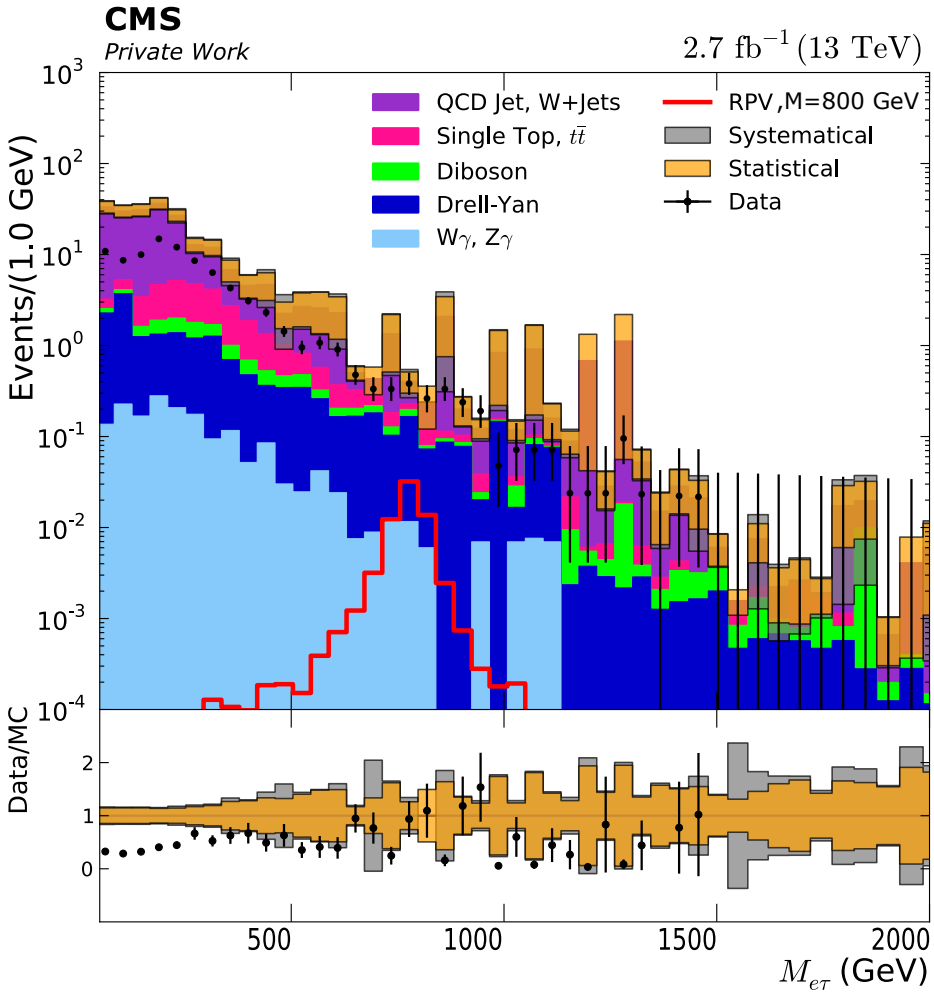

Figure 13: Distribution of invariant mass of the $e\tau$ pair in preselection stage. The binning is according to the mass resolution. Disagreement between data and MC for low masses is caused by inadequate simulation of QCD processes (see here fore Section 3.4.2).

4.3.1 *Opposite Sign Charged Leptons*

The electric neutral τ-sneutrino decays into a lepton pair of $e^{\pm}\tau^{\mp}$ where the electron and the tau are opposite charged due to conservation of electric charge. Therefore the electric charge of all reconstructed particles in the final state is multiplied. To pass these cut, an event is required to fulfill:

$$q_e \cdot q_\tau = -1 \tag{19}$$

This cut reduces the background by an order of magnitude (see also cut flow Figure 19) whereas the number of signal events is approximately unvaried. Mainly QCD events for lower invariant masses are reduced strongly as well as events of "Diboson" background processes for very small or high masses.
Figure 14a shows the invariant mass distribution of the $e\tau$ final state before the opposite sign requirement, whereas Figure 14b shows the distribution after the opposite sign requirement.

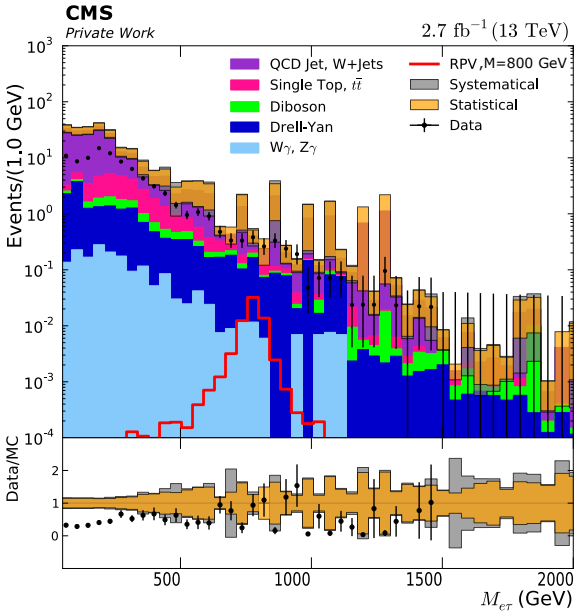

(a) $M_{e\tau}$ distribution before the opposite sign requirement.

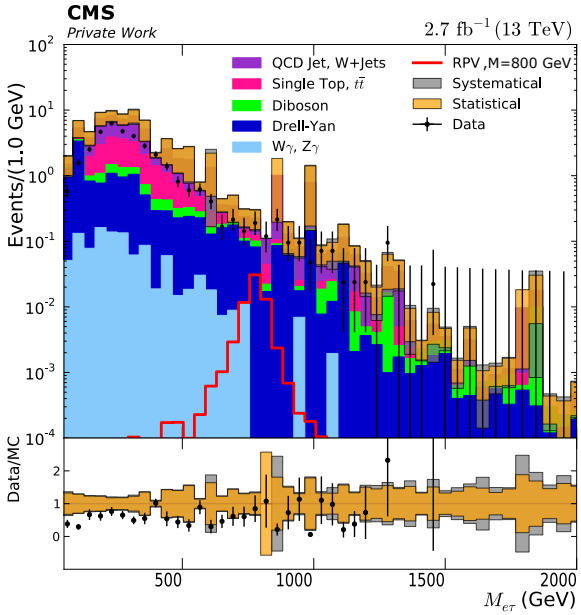

(b) $M_{e\tau}$ distribution after the opposite sign requirement.

Figure 14: Distribution of invariant mass of the $e\tau$ pair. The binning is according to the mass resolution. The signal is examplary for an invariant $e\tau$ mass of 800 GeV.

4.3.2 *B-Jet Veto*

Since the decay channel of the τ-sneutrino does not include b-quark jets, it is useful to veto events, which include them. Figure 15a shows the distribution of number of b-jets in an event. Especially $t\bar{t}$ and single top background events contain b-quark jets and can be reduced by the rejection of b-jets in $e\tau$ events. All the other cuts, used in this analysis, are already applied on the distribution in Figure 15a to demonstrate that a explicit b-jet veto is useful. Therefore the "pfCombinedSecondaryVertexV2BJetTags" algorithm [36], which was optimized for a center-of-mass energy of $\sqrt{s} = 13$ TeV, is used.

Analogous to the MVA-based isolation discriminator of Section 4.2.1, the b-jet identification algorithm is as well based on a multivariate analysis algorithm. Algorithms for b-jet identification use the relatively long life-time of b-mesons, which are part of jets outgoing from hadronized b-quarks. This long life-time results in a decay of the b-meson, displaced up to a few millimeters with respect to the primary interaction vertex. These secondary vertex may be reconstructed. The "Combined Secondary Vertex" algorithm (CVSv2) combines the information of measured tracks with the information of secondary vertices. Using a sequence of requirements for the tracks, particles and vertices, b-jets can be reconstructed.

Figure 15b shows the invariant mass distribution of the $e\tau$ final state after the applied opposite sign charged lepton cut and the b-jet veto. It is clearly recognizable, that most of the $t\bar{t}$ and single top background events were suppressed by these cut.

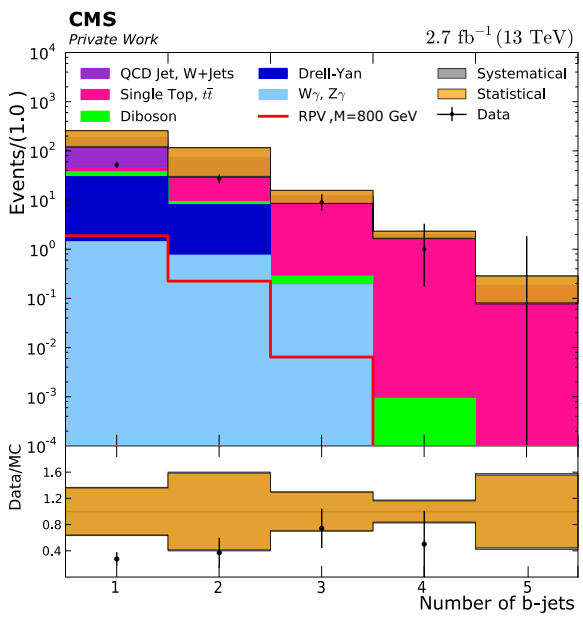

(a) Distribution of number of b-jets in a event. Except the b-jet veto, all other cuts used in this analysis are already applied at this stage, to demonstrate the effect of a b-jet veto independent of the overall cut sequence.

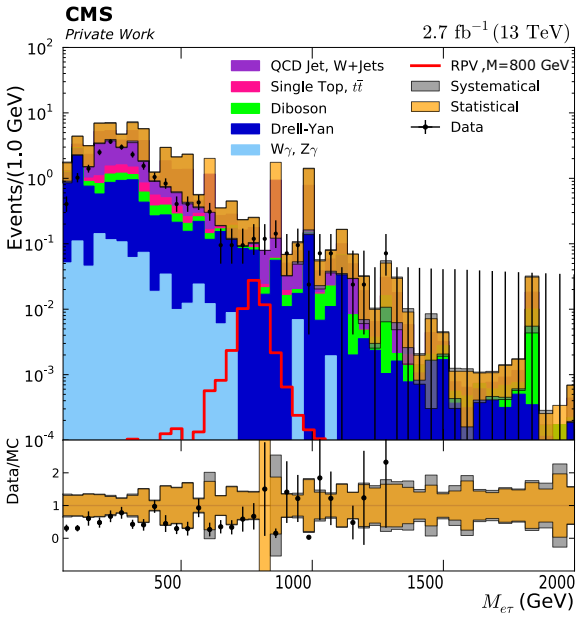

(b) $M_{e\tau}$ distribution after the opposite sign requirement and the b-jet veto.

Figure 15: Distribution of number of b-jets and distribution of invariant mass of the $e\tau$ pair. The binning of the $M_{e\tau}$ distribution is according to the mass resolution. The signal is examplary for an invariant $e\tau$ mass of 800 GeV.

4.3.3 *Angle between Tau and Missing Transverse Energy*

The final state of the decaying tau in the $e\tau$ resonance contains always a neutrino (see Table 5 for the dominant τ_h decay modes), which can be only reconstructed using missing transverse energy $\not{E}_T$ (see Section 4.3). The mesons, which are used to reconstruct the τ_h, and the neutrino are boosted almost in the same direction after the decay. This leads to an angular difference between the reconstructed τ_h and the neutrino close to zero. Figure 16a shows the distribution of this angle for background, signal and data events. The signal has a clear identifiable peak at zero and flattens for higher $\Delta\phi_{\tau,\not{E}_T}$, whereas the remaining background is approximately constant with $\Delta\phi_{\tau,\not{E}_T}$ since they are not dependent on these angle. All the other cuts, used in this analysis, are already applied on the distribution in Figure 16a to demonstrate the effect of a $\Delta\phi_{\tau,\not{E}_T}$ cut independent of the overall cut sequence. Since background and signal show a different characteristic to $\Delta\phi_{\tau,\not{E}_T}$, it is useful to cut on this variable.

For ten different cut values $\Delta\phi_{\tau,\not{E}_T}$ gradually increasing from 0.2 to 2.0, expected limits are calculated and shown in Figure 16c. The limit for $\Delta\phi_{\tau,\not{E}_T} = 0.4$ gives the best expected exclusion of cross section times branching ratio.
Therefore events in this analysis are required to have an angle between missing transverse energy and the reconstructed τ_h of lower than 0.4.

Figure 16b shows the distribution for invariant $e\tau$ mass after the $\Delta\phi_{\tau,\not{E}_T}$ cut. Especially Drell-Yan events and QCD events for high masses are suppressed by this cut.

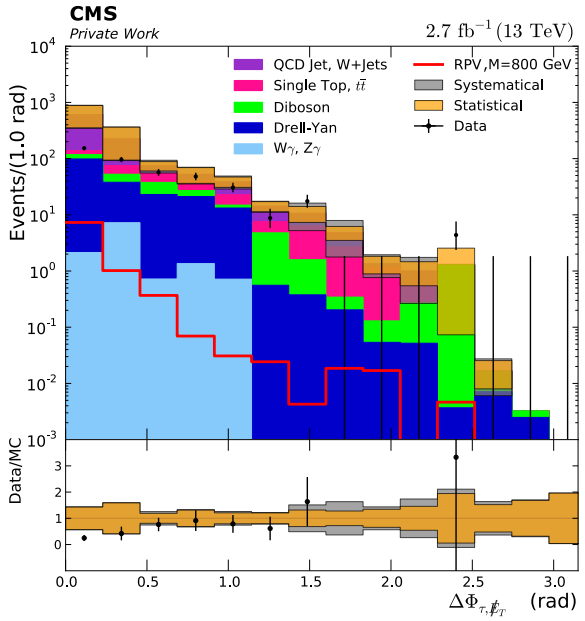

(a) Distribution of $\Delta\phi_{\tau,\not{E}_T}$. Except the cut on $\Delta\phi_{\tau,\not{E}_T}$, all other cuts used in this analysis are already applied at this stage, to demonstrate the effect of a $\Delta\phi_{\tau,\not{E}_T}$ cut independent of the overall cut sequence.

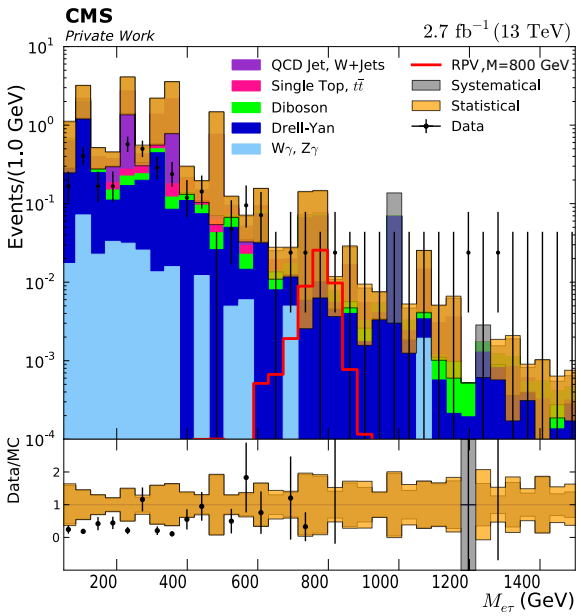

(b) $M_{e\tau}$ distribution after the opposite sign requirement, the b-jet veto and a cut on $\Delta\phi_{\tau,\not{E}_T} < 0.4$.

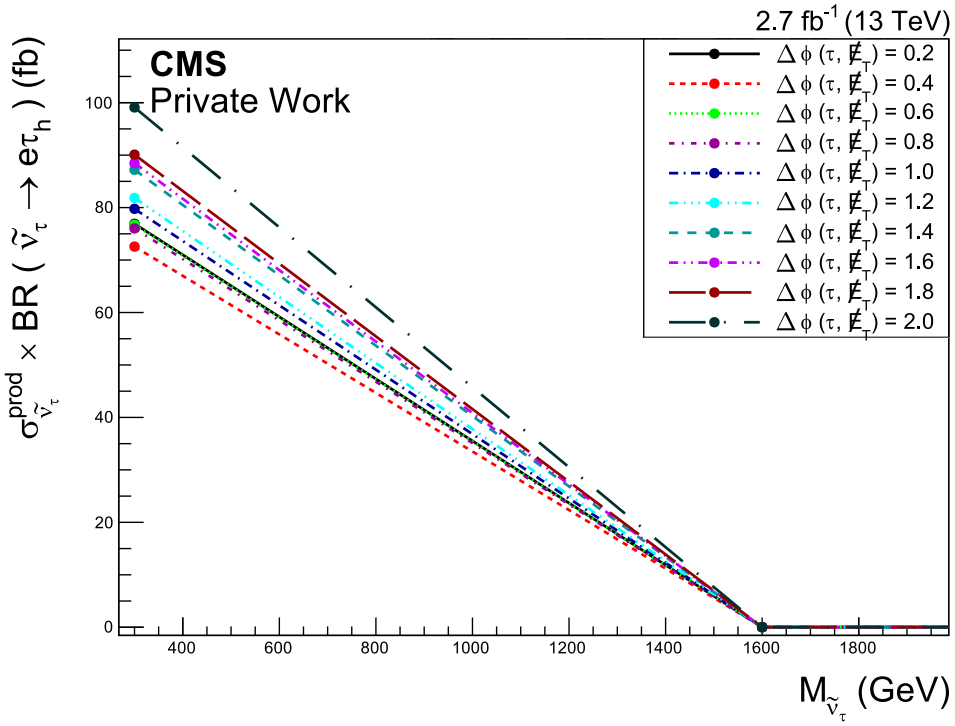

(c) Calculated expected limits on the cross section times branching ratio over the invariant mass of the τ-sneutrino for different cut values. The optimized cut requires $\Delta\phi_{\tau,\not{E}_T} < 0.4$. Since the expected upper limits for high masses are nearly steady for the used cut values, the line between the 1600 GeV and the 3500 GeV mass bin is horizontally constant. To enable a better overview, the range of the $\tilde{\nu}_\tau$ mass is limited to 2000 GeV.

Figure 16: Distribution of $\Delta\phi_{\tau,\not{E}_T}$ (a), invariant mass distriburion $M_{e\tau}$ after the $\Delta\phi_{\tau,\not{E}_T}$ cut (b), and calculated expected limits for cut optimization (c). The exemplary signal in (a) and (b) is according to an invariant mass of $M_{e\tau} = 800$ GeV.

4.3.4 *Angle between Tau and Electron*

Within the rest frame of the $\tilde{\nu}_\tau$, the tau's and electron's trajectories are back to back, due to conservation of momentum. The resulting angle between those particles is expected to be about π. Figure 17 shows the distribution of this angle for background, signal and data events. The signal increases with $\Delta\phi_{e,\tau}$ until a clear identifiable peak at π, whereas backgrounds events contain relatively more $e\tau$ events with smaller angle $\Delta\phi_{e,\tau}$. All the other cuts, used in this analysis, are already applied on the distribution in Figure 17 to demonstrate the effect of this cut being independent of the overall cut sequence. Since background and signal show a different characteristic to $\Delta\phi_{e,\tau}$, it is useful to cut on this variable.

For ten different cut values $\Delta\phi_{e,\tau}$ gradually increasing from 1.2 to 3.0, expected limits are calculated and shown in Figure 17c. The limit of $\Delta\phi_{e,\tau} = 2.8$ gives the best expected exclusion of cross section times branching ratio.
Therefore events in this analysis are required to have a minimum angle between the reconstructed electron and τ_h of 2.8.

Figure 17b shows the distribution for invariant $e\tau$ mass after the $\Delta\phi_{e,\tau}$ cut. Especially background events for low $e\tau$ masses are suppressed by this cut.

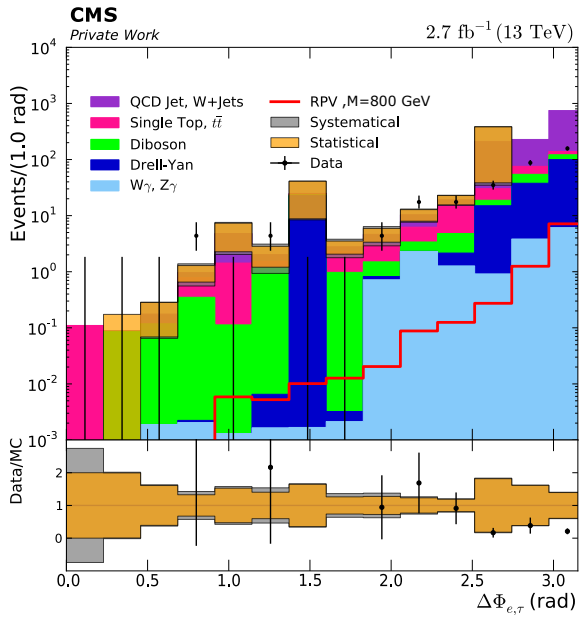

(a) Distribution of $\Delta\phi_{e,\tau}$. Except the cut on $\Delta\phi_{e,\tau}$, all other cuts used in this analysis are already applied at this stage, to demonstrate the effect of a $\Delta\phi_{e,\tau}$ cut independent of the overall cut sequence.

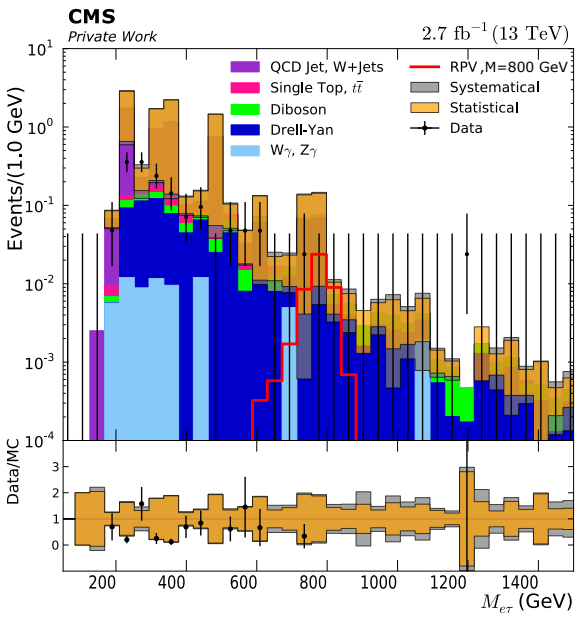

(b) $M_{e\tau}$ distribution after the opposite sign requirement, the b-jet veto, a cut on $\Delta\phi_{\tau,\not{E}_T} < 0.4$ and $\Delta\phi_{e,\tau} > 2.8$.

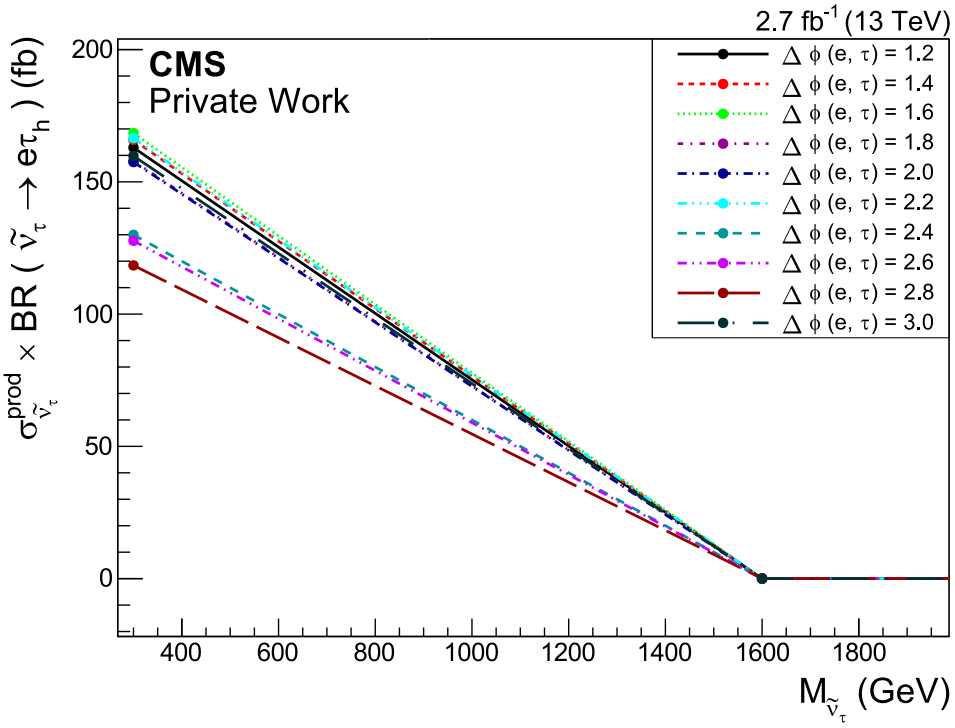

(c) Calculated expected limits on the cross section times branching ration over the invariant mass of the τ-sneutrino for different cut values. The optimized cut requires $\Delta\phi_{e,\tau} > 2.8$. Since the expected upper limits for high masses are nearly steady for the used cut values, the line between the 1600 GeV and the 3500 GeV mass bin is horizontally constant. To enable a better overview, the range of the $\tilde{\nu}_\tau$ mass is limited to 2000 GeV.

Figure 17: Distribution of $\Delta\phi_{e,\tau}$ (a), invariant mass distriburion $M_{e\tau}$ after the $\Delta\phi_{e,\tau}$ cut (b), and calculated expected limits for cut optimization (c). The exemplary signal in (a) and (b) is according to an invariant mass of $M_{e\tau} = 800$ GeV.

4.3.5 *Transverse Mass* M_T

The last cut is applied on the transverse mass M_T, which is calculated according to the electron and the neutrino. These quantity is defined by:

$$M_T = \sqrt{2E_T^e \not{E}_T (1 - \cos(\Delta\phi_{e,\not{E}_T}))} \tag{20}$$

Figure 18a shows the distribution of transverse mass for background, signal and data events. The signal increases strongly for a specific value of M_T, whereas the background is distributed along the whole range. It seems useful to cut on a minimum value of M_T to reduce especially background below these limit. All the other cuts, used in this analysis, are already applied on the distribution in Figure 18a to demonstrate the effect of this cut being independent of the overall cut sequence.

For ten different cut values, gradually increasing from $M_T = 50$ GeV to $M_T = 410$ GeV, expected limits are calculated and shown in Figure 18c. Limits for the highest three values do not appear in the graph, since there are no statistics of the signal left after the cut. Therefore cut values on M_T much higher than about 200 GeV are inadequate. The limit of $M_T > 130$ GeV gives the best expected exclusion of cross section times branching ratio.
Therefore events in this analysis are required to have a minimum transverse mass of 130 GeV according to definition in Equation 20.

Figure 18b shows the distribution for invariant $e\tau$ mass after the M_T cut.

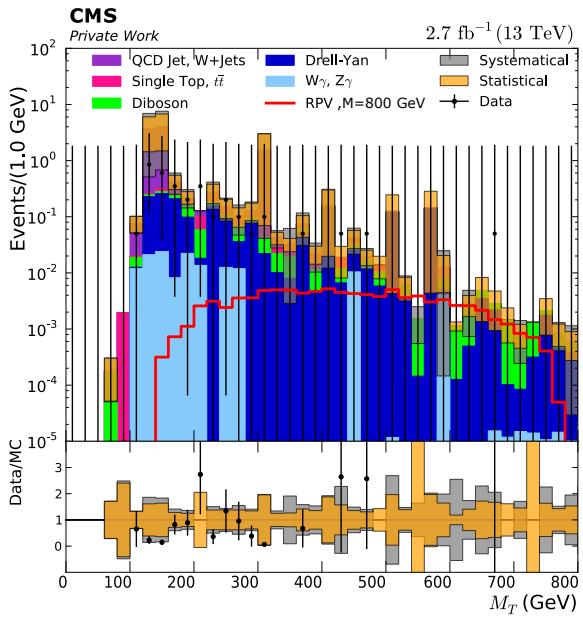

(a) Distribution of M_T. Except the cut on M_T, all other cuts used in this analysis are already applied at this stage, to demonstrate the effect of a M_T cut independent of the overall cut sequence.

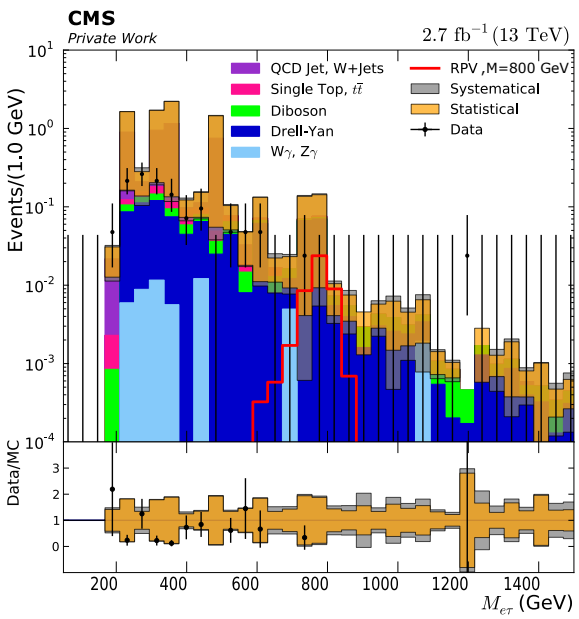

(b) $M_{e\tau}$ distribution after the opposite sign requirement, the b-jet veto, a cut on $\Delta\phi_{\tau,\not{E}_T} < 0.4$, $\Delta\phi_{e,\tau} > 2.8$ and on $M_T > 130$ GeV.

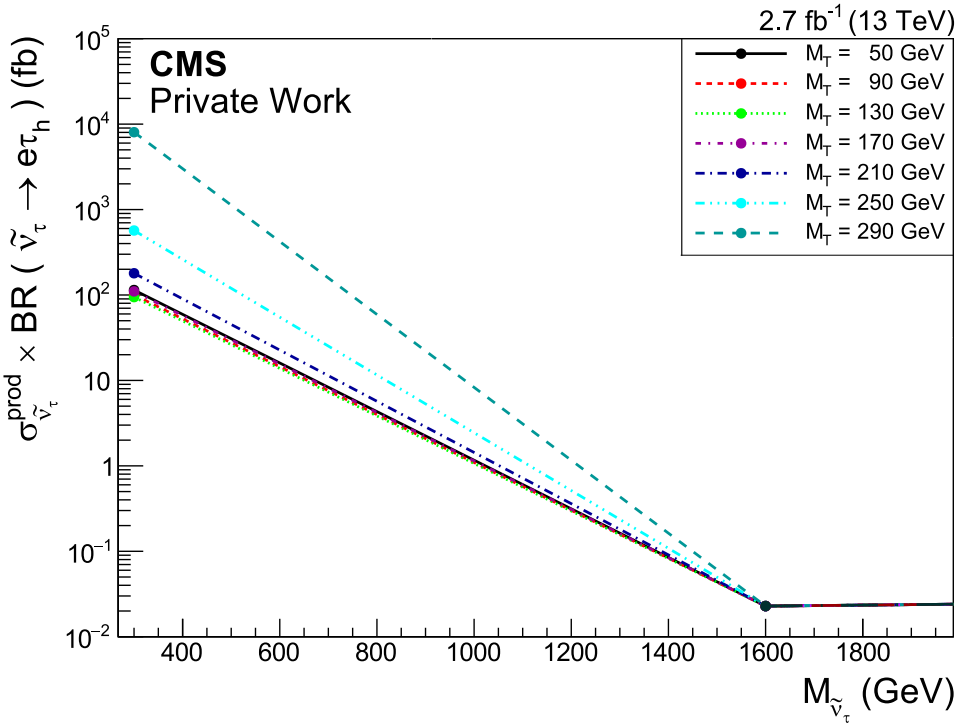

(c) Calculated expected limits on the cross section times branching ration over the invariant mass of the τ-sneutrino for different cut values. The optimized cut requires $M_T > 130$ GeV. Since the expected upper limits for high masses are nearly steady for the used cut values, the line between the 1600 GeV and the 3500 GeV mass bin is horizontally constant. To enable a better overview, the range of the $\tilde{\nu}_\tau$ mass is limited to 2000 GeV.

Figure 18: Distribution of M_T (a), invariant mass distriburion $M_{e\tau}$ after the M_T cut (b), and calculated expected limits for cut optimization (c). The exemplary signal in (a) and (b) is according to an invariant mass of $M_{e\tau} = 800$ GeV.

4.3.6 *Summary of Applied Kinematic Cuts*

Figure 19 shows the cumulated number of events in sequence of the requirements and applied cuts. The cut values and the concrete requirements are listed in Table 11 including the ratio of number of remaining background events after a certain requirement or kinematic cut within the sequence of requirements to the number of background events of preselection stage for different background processes.

The event selection criteria reduce the background events by two orders of magnitude, whereas the number of signal events of an exemplary signal with an invariant $e\tau$ mass of 800 GeV is only reduced to 65% of the preselection stage. The reduction of the number of signal events through the cut is correlated with the mass of the RPV signal. According to the cut values, signals of lower invariant $M_{e\tau}$ mass loose relatively less number of signal events compared to signals with high masses.

Although the number of QCD and W+jet events of the preselection stage are reduced to 1.51% with the kinematic cuts and requirements, these events still represent the dominant background with three fourth of the number of all background events. The disagreement between the number of data and background events, which is caused by QCD (Section 3.4.2), still remains.

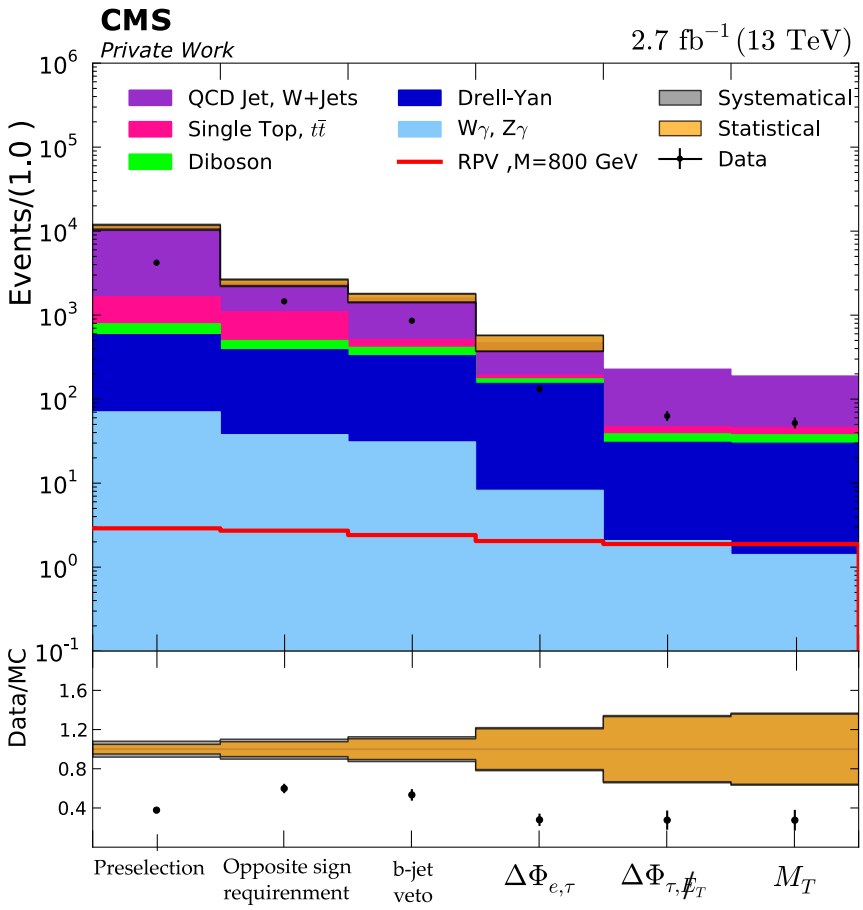

Figure 19: Cumulated number of events in sequence of applied cuts or event requirements.

Table 11: List of event criteria, the corresponding cut values or requirements and ratios of background processes in percent. The ratio of a background process is given by the ratio of number of remaining background events after a certain requirement or kinematic cut within the sequence of requirements to the number of background events of preselection stage. The ratio is calculated analogously and given for a exemplary signal of 800 GeV.

Event criteria	Cut value / requirement	QCD, W+Jets	Single Top, $t\bar{t}$	Di-boson	Drell-Yan	W_γ, Z_γ	RPV signal of 800 GeV
Opposite sign requirement	$q_e \cdot q_\tau = -1$	14.1	67.7	55.8	67.6	53.6	93.8
B-jet veto	$N_{b-jets} = 0$	11.6	11.0	42.6	57.6	43.9	83.1
Angle between τ and $\not{E}_T$	$\Delta\phi_{\tau,\not{E}_T} < 0.4$	3.0	2.1	10.1	28.1	11.7	70.6
Angle between τ and e	$\Delta\phi_{e,\tau} > 2.8$	1.9	1.0	4.0	5.6	3.0	65.0
Transverse mass	$M_T > 130$ GeV	1.5	0.9	3.8	5.5	2.0	65.0

4.4 SIGNAL EFFICIENCY

The selection criteria for the electron and the τ_h, which are described in Section 4.1 and Section 4.2, are used to reconstruct $e\tau$ events. Further requirements and kinematic cuts are applied to select RPV signal events from SM background processes (Section 4.3). Figure 20 shows various efficiencies, which prerequisite different event criteria within the analysis. All efficiencies only consider hadronically decaying taus.

The acceptance describes the signal acceptance, which fulfills the limits of transverse momentum $p_T > 20$ GeV and pseudorapidity $|\eta| < 2.3$ due to the requirements of Section 4.2. For signal events with high $e\tau$ invariant mass, the acceptance is above 90%.

The trigger efficiency requires $e\tau$ events, which fulfill the p_T and η limits and furthermore are selected by the trigger (described in Section 4.1.1).

The preselection efficiency is the efficiency of finding and reconstructing an $e\tau$ event, using all selection criteria for electrons and taus, whereas no requirements or kinematic cut criteria of signal event selection (Section 4.3) are required.

The final selection efficiency includes all criteria and cuts, which are finally used to select RPV resonant signal events. For signal events above the turn-on-region up to 1500 GeV the final $e\tau$ selection efficiency is stable around 25% to 30%. For limit calculation at arbitrary signal masses, a function is fitted to the final selection efficiency with the following parameterization:

$$\epsilon_{e\tau} = A + \frac{B}{C + M^{gen}_{e,\tau}} + D \cdot M^{gen}_{e,\tau} \tag{21}$$

where $M^{gen}_{e,\tau}$ is the generated invariant mass of an $e\tau$ pair. The values of the coefficients A, B, C, D are given in Figure 20 below.

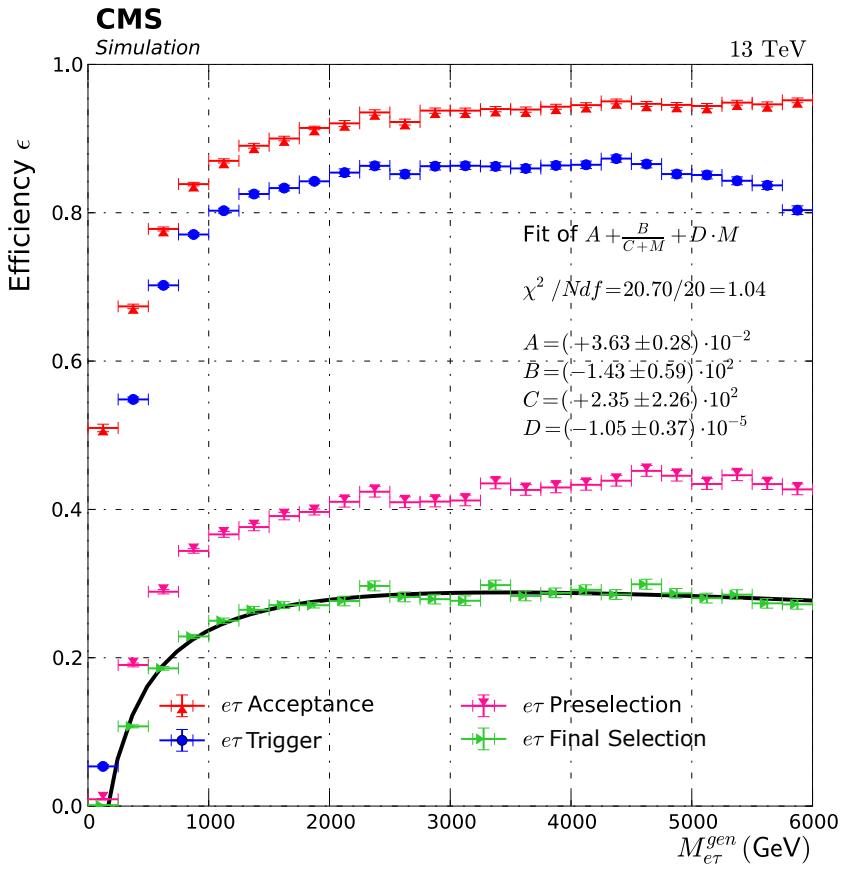

Figure 20: Efficiency of the RPV signal after the acceptance requirements (red points), after the acceptance and trigger requirements (dark blue points), after the preselection requirenments including acceptance, trigger, electron and tau cirteria but excluding any signal event criterea (pink points) and after the final selection including acceptance, trigger, electron, tau and signal event criteria (light green points).

4.5 eτ INVARIANT MASS RESOLUTION

The relative per-event mass resolution describes the discrepancy of invariant mass of eτ pairs between generated and reconstructed events and is defined by

$$\sigma_{e\tau} = \frac{(M^{reco}_{e\tau} - M^{gen}_{e\tau})}{M^{gen}_{e\tau}} \tag{22}$$

The invariant mass resolution is calculated for each single event of one signal mass point. Per signal mass bin, the resulting distribution is fitted with a Gaussian and a Crystal Ball fit around the mean of the distribution. The fit function is chosen according to the smallest resulting χ^2 value. A Gaussian fit for the signal mass point of 800 GeV is shown exemplary in Figure 21. The width σ of the Gaussian or the Crystall Ball fit is the measure of the mass resolution. The resulting relative mass resolution of eτ pairs after the application of all signal event selection criteria is shown in Figure 22a. It consists of 23 points, which are fitted by the following function

$$f_{res} = A + B \cdot M^{gen}_{e\tau} + C \cdot (M^{gen}_{e\tau})^2 + D \cdot (M^{gen}_{e\tau})^3 + E \cdot (M^{gen}_{e\tau})^4 + \frac{F}{M^{gen}_{e\tau}} \tag{23}$$

The values of the coefficients A, B, C, D, E and F are given in the plot for the efficiency shown in Figure 22a. The mass resolution becomes worse with invariant mass lower than 2 TeV and higher than 5 TeV with a plateau in between. The shape of the mass distribution is correlated to the resolution of transverse momentum of the electron and tau. These relative per-event resolutions describe the discrepancy of p_T between generated and reconstructed events and are defined by

$$\sigma_{p_T} = \frac{(p^{reco}_T - p^{gen}_T)}{p^{gen}_T} \tag{24}$$

The p_T resolution is calculated analogously to the invariant mass resolution. Figure 22b and Figure 22c show the p_T resolution of the electron and the τ_h after the application of all signal event selection criteria as a function of the generated particle's momentum. The p_T resolution is fitted analogous to the invariant mass distribution. The used function and the values of the coefficients A, B, C and D are given in the related resolution plot.

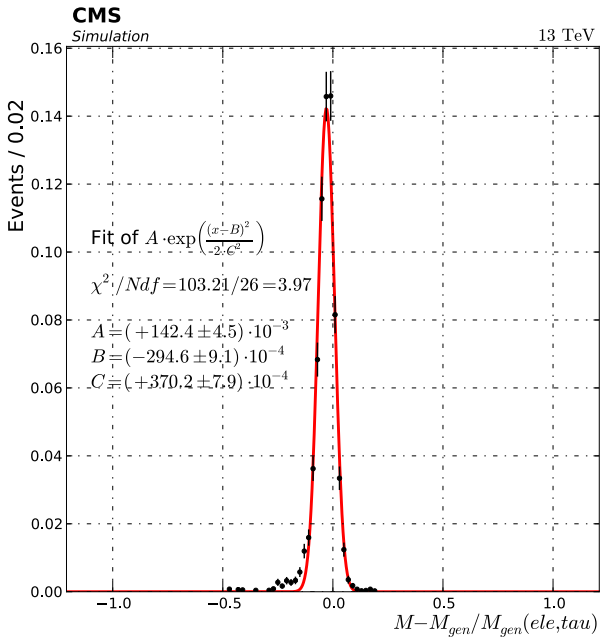

Figure 21: Exemplary Gaussian fit of invariant eτ mass point of 800 GeV. The width C is used in Figure 22a as the measure of the 800 GeV mass bin's resolution.

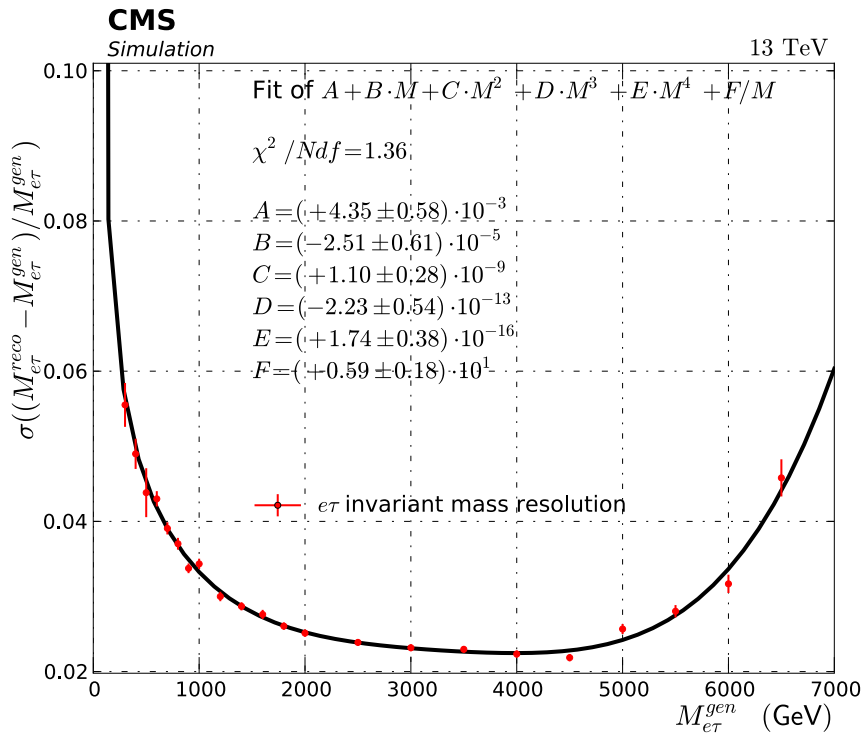

(a) Relative invariant mass resolution of eτ pairs, obtained from signal simulation after the application of all signal event selection criteria.

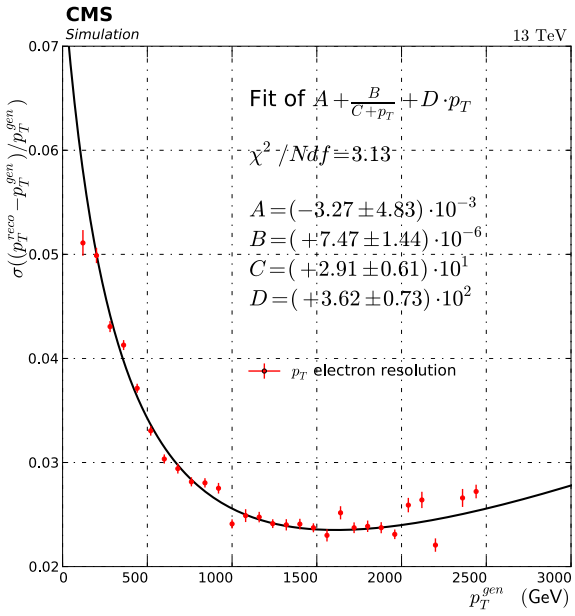

(b) Relative transverse momentum resolution of the electron, obtained from signal events after the application of all signal event selection criteria.

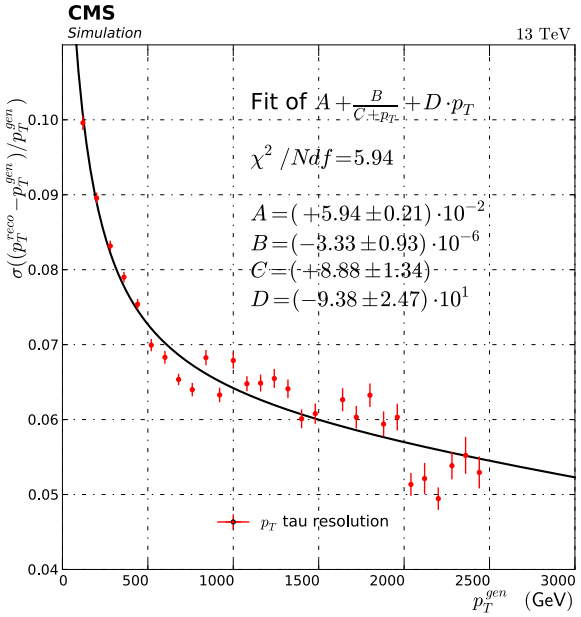

(c) Relative transverse momentum resolution of the τ_h, obtained from signal events after the application of all signal event selection criteria. Here the missing transverse energy of the hadronically decaying tau is not considered in the p_T.

Figure 22: Invariant mass resolution of eτ pairs and transverse momentum resolution of the electron and the hadronic parts of the hadronically decaying tau within the signal events.

The p_T resolution of the electron and tau becomes better with higher p_T due to the fact that the calorimeters get stronger signals and their resolution increases until a saturation plateau is reached (see also Equation 5 and Equation 6). With higher p_T the electron's resolution decreases with the silicon tracker resolution, since the electron's trajectory is less bend (see also Equation 4).

4.6 SYSTEMATICAL UNCERTAINTIES

For this analysis different systematic uncertainties are taken into account. The following systematic uncertainties are used for background processes [37]

- The electron and tau p_T scale is used for the background event rate. The electron transverse momentum is shifted by 0.4% for electrons in the barrel and by 0.8% for electrons in the endcap. The tau transverse momentum scale is shifted by 3%.
- Scale factors are applied for electrons, that pass the HEEP ID (Section 4.1.2). The scale factors and the corresponding systematic uncertainty is taken from [38].
- Lowered kinematic cuts are used for systematic uncertainties, to allow particles shift from selected to selected. Concrete lowered kinematic cut values are

  The minimum of the electron's transverse momentum is shifted to $p_T > 15$ GeV.

  The boundaries of the electron's pseudorapidity are shifted to $1.56 < \eta < 2.8$ in the endcap and $|\eta| > 1.442$ in the barrel.
- The uncertainty on pile-up events is estimated by a $\pm 5\%$ shift of the minimum bias cross section.
- A systematic uncertainty of 2.7% is assigned to the integrated luminosity and is used for background rates.

4.7 STATISTICAL INTERPRETATION

4.7.1 *Limit Calculation*

The statistical analysis of the RPV model is performed using a Bayesian approach [39]. The Bayesian approach is based on the Bayes' theorem, which describes conditional probability.

$$P(\text{theory}|\text{data}) \propto P(\text{data}|\text{theory}) \cdot P(\text{theory}) \tag{25}$$

were $P(\text{theory}|\text{data})$ is the probability of observing N events in data, which are expected by theory. Based on that theorem, the posterior probability density function, which is used to calculate, if the model describes the data properly, is given by

$$P(s|N) = \frac{L(N|s) \cdot \pi(s)}{\int L(N|s') \cdot \pi(s') ds'} \tag{26}$$

where $L(N|s)$ is the Likelihood function and $\pi(s)$ the prior probability, if the model is accurate. The parameter s denotes the number of signal events and b the number of background events in case of an experiment with N Poisson distributed data events. Due to the Poisson distribution, the Likelihood function is regarded as

$$L(s|N) = \frac{(s+b)^N}{N!} \cdot e^{-(s+b)} \tag{27}$$

Furthermore an upper limit on the number of signal events u can be computed according to a confidence level of 95% by integration

$$0.95 = \int_{-\infty}^{u} P(s|N) \tag{28}$$

An advantage of using Bayesian statistics for limit calculation is the option to include additional "a priori" information.

In this analysis the only prior information used, is the requirement of a positive cross section times branching ratio for the researched signal event. The RPV signals result in a narrow resonance. Since the width σ of the signals is small compared to the detector resolution (see Section 2.2) and tails are small, a Gaussian curve is used to model the signal shape. Here, the width σ is taken from the fit to the invariant mass resolution as described in Section 4.5. Histograms are constructed from the Gaussian signal particle density function and they are normalized to the expected number of signal events, given by the signal cross section, integrated luminosity and final selection efficiency. Here the fit of the final selection efficiency as described in Section 4.4 was used. The parameterization of the narrow resonance allows a scan of the invariant mass spectrum with a fine spacing of the signal mass. Therefore the hypothesis corresponds to the invariant mass resolution.

No excess with respect to the expectation is found in the measured invariant mass distribution shown in Figure 23. Therefore exclusion limits on the signal cross section with a 95% confidence level are determined. Here the multibin limit setting tool developed by the Higgs group [40] was used.
The multibin limit is derived using binned $e\tau$ mass histograms as input [37].

4.7.2 *Results on RPV Resonant $\tilde{\nu}_\tau$*

The $e\tau$ invariant mass distributions of the data, signal and background processes except the QCD samples were used for the limit calculation after all event selection criteria were applied. The invariant mass distribution including the QCD samples is shown in Figure 23. The disagreement between data and background is caused by inappropriate simulated QCD Monte Carlo samples (Section 3.4.2), which evoke high spikes of statistical uncertainties. These lead to problems within the limit calculation procedure and therefore the QCD Monte Carlo samples have to be excluded for the limit calculation.

The limits were calculated by Ms. Swagata Mukherjee. Figure 24 shows the limit on the cross section times branching ratio of the RPV resonant tau sneutrino production and decay into a electron plus tau pair. The solid black line represents the observed limit, given by the CMS data, recorded in year 2015 with a luminosity of 2.7 fb^{-1}. The dashed black line represents the expected limit, given by the simulation of expected SM processes. The yellow and green bounds represent the one and two sigma uncertainties of the expected limit. The observed limit is within the two sigma expectation range for $e\tau$ masses above 200 GeV with an exception at a mass of 1200 GeV. This is due to a local disagreement between data and background, which is also noticeable in the mass distribution.

The red line represents the cross section times branching ratio given by the theory with the used couplings. As a result a tau sneutrino with a mass below 650 GeV and couplings of $\lambda' = \lambda_{313} = \lambda_{331} = 0.01$ can be excluded.

4.7.3 *Comparison with analysis from ATLAS*

The ATLAS collaboration has performed this analysis with 8 TeV data using 20.3 fb^{-1} luminosity [41]. The resulting limits are set on the cross section of the production of a $\tilde{\nu}_\tau$, decaying into the R-parity violating resonance in $e^{\pm}\tau^{\pm}$ final state. Candidate signal events within the ATLAS analysis are required to have exactly two leptons, of opposite charge and of different flavor. Analogously only hadronically decaying taus are used for tau reconstruction. Candidate signal events need to satisfy lepton selection criteria of $E_T > 25$ GeV for the τ_h and the electron, where the E_T of the τ_h candidate is required to be less than the E_T of the electron. Furthermore kinematic cuts on $\Delta\phi_{e\tau} > 2.7$, $\not{E}_T < 30$ GeV and $p_T^{\text{electron}} < 150$ GeV were applied. For the couplings of $\lambda'_{311} = 0.11$ and $\lambda_{313} = \lambda_{331} = 0.07$ a lower limit on the $\tilde{\nu}_\tau$ mass of 1.7 TeV is given. The numbers of observed candidate events are compatible with the SM expectations.

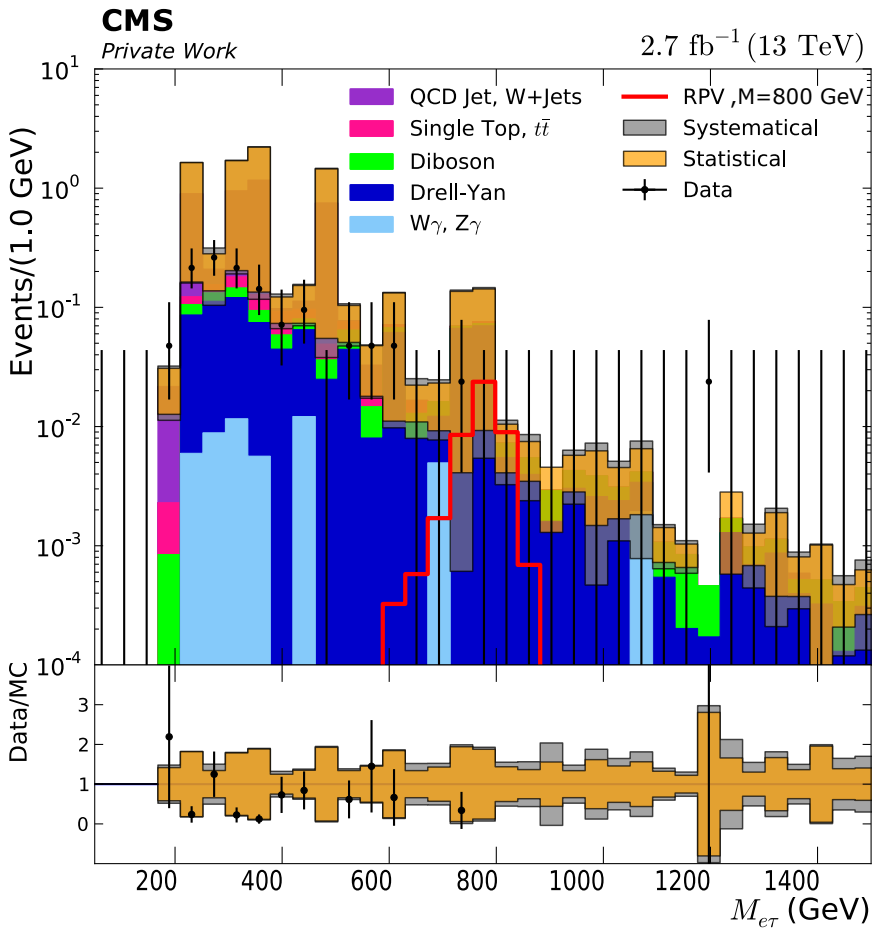

Figure 23: $M_{e\tau}$ distribution after all event selection criteria were applied. The exemplary signal in this distribution is according to an invariant mass of $M_{e\tau} = 800$ GeV.

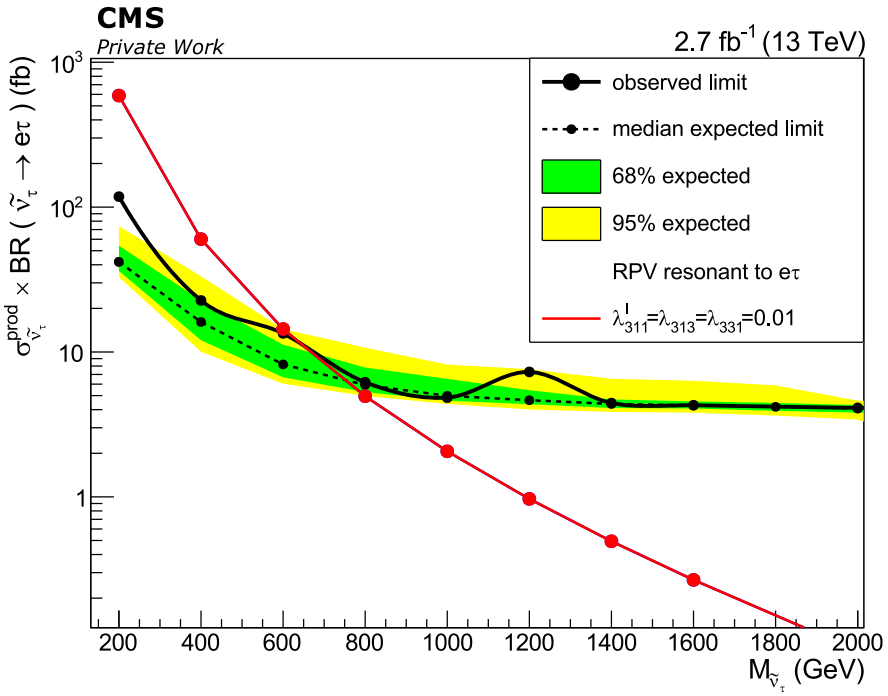

Figure 24: Cross section times branching ratio as a function of the tau sneutrino mass.

5 CONCLUSION

In this analysis a search for R-parity violating resonant production of a SUSY tau sneutrino and decay into an electron plus tau pair has been performed. Therefore single electron events, recorded within pp-collisions by CMS with a center of mass energy of $\sqrt{s} = 13$ TeV and a luminosity of $\mathcal{L}_{int} \approx 2.7$ fb^{-1} were used. Event selection criteria were discussed and chosen. The number of background events was reduced by two orders of magnitude using optimized kinematic cuts and signal requirements. Inappropriate Monte Carlo simulation of QCD processes leads to a disagreement between data and background events, but with neglect of these, no significant excess of data has been observed in comparison to the Standard Model's prediction. Therefore limits on the cross section times branching ratio of the tau sneutrino production and decay into an $e\tau$ pair were calculated by Ms. Swagata Mukherjee. The production and decay into an $e\tau$ pair of a tau with a mass below 650 GeV and couplings of $\lambda' = \lambda_{313} = \lambda_{331} = 0.01$ can be excluded.

APPENDIX

Table 12: Used RPV signal Monte Carlo samples of different values for the invariant mass of the resonance $M_{\tilde{\nu}_\tau}$. Each sample contains 15000 generated events. The cross section times branching ratio (BR) is given for each sample. The RPV signal cross section is calculated at NLO in perturbative QCD. Taken from [42] , [43]

$M_{\tilde{\nu}_\tau}$ (GeV)	$\sigma\cdot$ BR ($\tilde{\nu}_\tau \to e^{\pm}\tau^{\pm}$) (fb)	$M_{\tilde{\nu}_\tau}$ (GeV)	$\sigma\cdot$ BR ($\tilde{\nu}_\tau \to e^{\pm}\tau^{\pm}$) (fb)
200	$5.88 \cdot 10^{2}$	1800	$1.49 \cdot 10^{-1}$
300	$1.57 \cdot 10^{2}$	2000	$8.66 \cdot 10^{-2}$
400	$6.01 \cdot 10^{1}$	2500	$2.40 \cdot 10^{-2}$
500	$2.90 \cdot 10^{1}$	3000	$7.08 \cdot 10^{-3}$
600	$1.44 \cdot 10^{1}$	3500	$2.13 \cdot 10^{-3}$
700	8.20	4000	$6.41 \cdot 10^{-4}$
800	4.95	4500	$1.85 \cdot 10^{-4}$
900	3.13	5000	$5.18 \cdot 10^{-5}$
1000	2.06	5500	$1.36 \cdot 10$—5
1200	$9.68 \cdot 10^{-1}$	6000	$3.34 \cdot 10^{-6}$
1400	$4.94 \cdot 10^{-1}$	6500	$7.81 \cdot 10^{-7}$
1600	$2.67 \cdot 10^{-1}$	-	-

Table 13: Used background Monte Carlo samples with corresponding generator, kinematic cuts, used cross section with corresponding order and number of generated events taken from [42] , [43].

PROCESS	GENERATOR	KINEMATIC CUTS (GeV)	σ_{used} (pb)	$N^{\text{gen}}_{\text{events}}$ (10^6)
$W\text{Jets} \to l\nu$	madgraphMLM	$M < 100$	$6.15 \cdot 10^{4}$ (NLO)	47.16
$W\text{Jets} \to l\nu$	madgraphMLM	$100 < M < 200$	$1.63 \cdot 10^{3}$ (NLO)	28.38
$W\text{Jets} \to l\nu$	madgraphMLM	$200 < M < 400$	$4.35 \cdot 10^{2}$ (NLO)	14.93
$W\text{Jets} \to l\nu$	madgraphMLM	$400 < M < 600$	$5.92 \cdot 10^{1}$ (NLO)	1.94
$W\text{Jets} \to l\nu$	madgraphMLM	$600 < M < 800$	$1.46 \cdot 10^{1}$ (NLO)	3.77
$W\text{Jets} \to l\nu$	madgraphMLM	$800 < M < 1200$	6.66 (NLO)	0.05
$W\text{Jets} \to l\nu$	madgraphMLM	$1200 < M < 2500$	1.61 (NLO)	0.25
$W\text{Jets} \to l\nu$	madgraphMLM	$M > 2500$	$3.89 \cdot 10^{-2}$ (NLO)	0.25
$W\gamma \to l\nu\gamma$	madgraph	$M < 500$	$5.00 \cdot 10^{2}$ (LO)	6.10
$W\gamma \to l\nu\gamma$	madgraph	$M > 500$	$1.18 \cdot 10^{-2}$ (LO)	1.39
$Z\gamma \to ll\gamma$	aMC@NLO	-	$1.18 \cdot 10^{2}$ (LO)	4.33
$Z \to ee$	powheg	$50 < M_{ee} < 120$	$1.98 \cdot 10^{3}$ (NLO)	2.98
$Z \to ee$	powheg	$120 < M_{ee} < 200$	$1.93 \cdot 10^{1}$ (NLO)	0.10
$Z \to ee$	powheg	$200 < M_{ee} < 400$	2.73 (NLO)	0.10
$Z \to ee$	powheg	$400 < M_{ee} < 800$	$2.41 \cdot 10^{-1}$ (NLO)	0.10
$Z \to ee$	powheg	$800 < M_{ee} < 1400$	$1.68 \cdot 10^{-2}$ (NLO)	0.10
$Z \to ee$	powheg	$1400 < M_{ee} < 2300$	$1.39 \cdot 10^{-3}$ (NLO)	0.10
$Z \to ee$	powheg	$2300 < M_{ee} < 3500$	$8.95 \cdot 10^{-5}$ (NLO)	0.10
$Z \to ee$	powheg	$3500 < M_{ee} < 4500$	$4.14 \cdot 10^{-6}$ (NLO)	0.10
$Z \to ee$	powheg	$4500 < M_{ee} < 6000$	$4.56 \cdot 10^{-7}$ (NLO)	0.10
$Z \to ee$	powheg	$M_{ee} > 6000$	$2.07 \cdot 10^{-8}$ (NLO)	0.10

PROCESS	GENERATOR	KINEMATIC CUTS (GeV)	σ_{used} (pb)	N^{gen}_{events} (10^6)
DYJets $\to \tau\tau$	aMC@NLO	$50 < M_{\tau\tau} < 100$	$6.10 \cdot 10^{3}$ (NLO)	28.75
DYJets $\to \tau\tau$	aMC@NLO	$100 < M_{\tau\tau} < 200$	$2.26 \cdot 10^{2}$ (NLO)	0.10
DYJets $\to \tau\tau$	aMC@NLO	$200 < M_{\tau\tau} < 400$	7.67 (NLO)	0.01
DYJets $\to \tau\tau$	aMC@NLO	$400 < M_{\tau\tau} < 500$	$4.23 \cdot 10^{-1}$ (NLO)	0.01
DYJets $\to \tau\tau$	aMC@NLO	$500 < M_{\tau\tau} < 700$	$2.40 \cdot 10^{-1}$ (NLO)	0.01
DYJets $\to \tau\tau$	aMC@NLO	$700 < M_{\tau\tau} < 800$	$3.50 \cdot 10^{-2}$ (NLO)	0.01
DYJets $\to \tau\tau$	aMC@NLO	$800 < M_{\tau\tau} < 1000$	$3.00 \cdot 10^{-2}$ (NLO)	0.01
DYJets $\to \tau\tau$	aMC@NLO	$1000 < M_{\tau\tau} < 1500$	$1.60 \cdot 10^{-2}$ (NLO)	0.01
DYJets $\to \tau\tau$	aMC@NLO	$1500 < M_{\tau\tau} < 2000$	$2.00 \cdot 10^{-3}$ (NLO)	0.01
DYJets $\to \tau\tau$	aMC@NLO	$2000 < M_{\tau\tau} < 3000$	$5.40 \cdot 10^{-4}$ (NLO)	0.01
$t\bar{t}$	powheg	$M < 700$	$8.32 \cdot 10^{2}$ (NNLO)	97.90
$t\bar{t}$	powheg	$700 < M < 1000$	$7.66 \cdot 10^{1}$ (NNLO)	3.04
$t\bar{t}$	powheg	$1000 < M$	$2.58 \cdot 10^{1}$ (NNLO)	1.78
$tW \to 2l2\nu b$	powheg	-	$3.81 \cdot 10^{1}$ (NNLO)	0.49
$\bar{t}W \to 2l2\nu\bar{b}$	powheg	-	$3.56 \cdot 10^{1}$ (NNLO)	1.00
$tq \to l\nu bq$	powheg	-	$4.19 \cdot 10^{1}$ (NNLO)	3.09
$\bar{t}q \to l\nu\bar{b}q$	powheg	-	$2.53 \cdot 10^{1}$ (NNLO)	1.63
$WW \to 2l2\nu$	powheg	$M < 200$	$1.22 \cdot 10^{1}$ (NNLO)	1.98
$WW \to 2l2\nu$	powheg	$200 < M < 600$	1.39 (NNLO)	0.20
$WW \to 2l2\nu$	powheg	$600 < M < 1200$	$5.67 \cdot 10^{-2}$ (NNLO)	0.20
$WW \to 2l2\nu$	powheg	$1200 < M < 2500$	$3.57 \cdot 10^{-3}$ (NNLO)	0.20
$WW \to 2l2\nu$	powheg	$2500 > M$	$1.22 \cdot 10^{1}$ (NNLO)	0.04
$WW \to 4q$	powheg	-	5.17 (NNLO)	2.00
$WW \to l\nu qq$	powheg	-	$5.00 \cdot 10^{-1}$ (NNLO)	0.04
$ZZ \to 2l2\nu$	powheg	-	$5.64 \cdot 10^{-1}$ (NLO)	8.71
$ZZ \to 4l$	powheg	-	1.26 (NLO)	6.67
$ZZ \to 2l2q$	aMC@NLO	-	3.22 (NLO)	15.26
$ZZ \to 3l\nu$	aMC@NLO	-	4.43 (NLO)	2.00
$WZ \to l\nu 2q$	madgraph	-	9.81 (NLO)	2.00
$WZ \to 3l\nu$	powheq	-	4.43 (NLO)	2.00
$WZ \to 2l2q$	aMC@NLO	-	5.60 (NLO)	25.21
QCD EM-Enriched	pythia8	$50 < M < 80$	$1.98 \cdot 10^{7}$ (LO)	22.22
QCD EM-Enriched	pythia8	$80 < M < 120$	$2.80 \cdot 10^{6}$ (LO)	36.03
QCD EM-Enriched	pythia8	$120 < M < 170$	$4.77 \cdot 10^{5}$ (LO)	36.20
QCD EM-Enriched	pythia8	$170 < M < 300$	$1.14 \cdot 10^{5}$ (LO)	11.52
QCD EM-Enriched	pythia8	$300 < M$	$1.35 \cdot 10^{3}$ (LO)	7.34

BIBLIOGRAPHY

1. W. Demtröder. *Machanik und Wärmelehre* (Springer Spektrum, 2015).
2. C. Berger. *Elementarteilchenphysik. Von den Grundlagen zu den modernen Experimenten* 3rd ed. (Springer Spektrum Heidelberg, 2014).
3. C. Gerthsen, H. Vogel & Dieter Meschede. *Gerthsen Physik : Die ganze Physik zum 21. Jahrhundert* 23rd ed. (Springer Verlag, 2006).
4. M. Gell-Mann. A schematic model of baryons and mesons. *Phys. Rev. Lett.* 1964. http://linkinghub.elsevier.com/retrieve/pii/S0031916364920013 ((July 2016)).
5. Prof. Dr. L. Feld. *Vorlesungsskript zur Veranstaltung: Experimentalphysik Vb. Teilchen- und Astrophysik.* (RWTH Aachen 2015, 2016).
6. Particle Data Group. *Standard Model of Elementary Particles* https://commons.wikimedia.org/wiki/File:Standard_Model_of_Elementary_Particles.svg (Fermilab, Office of Science, United States Department of Energy, 27th June 2006).
7. A. Brignole, F. Feruglio & F. Zwirner. Four-fermion interactions and sgoldstino masses in models with a superlight gravitino. *CERN-TH/98-149, DFPD-98/TH/20.* https://arXiv:hep-ph/9805282v2, 9 (31. August 1998).
8. W. Demtröder. *Kern-, Teilchen- und Astrophysik* 2nd ed., 180 (Springer Spektrum, 2005).
9. DPG particle data group. *Particle Physics Booklet. Chinese Physics C* July 2014.
10. ATLAS & The CMS Collaboration. Combined Measurement of the Higgs Boson Mass in pp Collisions at $\sqrt{s} = 7$ and 8 TeV with the ATLAS and CMS Experiments. *Phys. Rev. Lett.* 191803. https://arxiv.org/abs/1503.07589, 114 (March 2015).
11. NASA Science: Astrophysics. *Dark Energy, Dark Matter* [web article]. http://science.nasa.gov/astrophysics/focus-areas/what-is-dark-energy/ (15th June 2016).
12. S. P. Martin. A Supersymmetry Primer. *High Energy Physics.* https://arxiv.org/abs/hep-ph/9709356 (1997).
13. Y. Shirman. TASI 2008 Lectures: Introduction to Supersymmetry and Supersymmetry Breaking. *High Energy Physics* (2009).
14. H. K. Dreiner, C. Luhn, H. Murayama & M. Thormeier. Baryon Triality and Neutrino Masses from an Anomalous Flavor $\mathrm{U}(1)$. *Nucl.Phys.B774* 127-167. https://arXiv:hep-ph/0610026 (2007).
15. CERN press office. *LHC Season 2: facts & figures* [web article]. http://press.cern/backgrounders/lhc-season-2-facts-figures (15th June 2016).
16. C. Lefevre. *The CERN accelerator complex* [schematic depiction]. http://www.stfc.ac.uk/stfc/includes/themes/MuraSTFC/assets/legacy/LHCinteractive/LHC_default.jpg. 2008.

17. D. Teyssier. CMS detector performance. *EPF Web of Conferences* 70, 00028. http://www.epj-conferences.org/articles/epjconf/pdf/2014/07/epjconf_icfp2012_00028.pdf (2014).
18. K. Hoepfner. CMS upgrade and future plans. *WPJ Web of Conferences* 95,03016. http://www.epj-conferences.org/articles/epjconf/pdf/2015/14/epjconf_icnfp2014_03016.pdf (2016).
19. Int. Particle Physics Outreach Group. *CMS Slice* [schematic depiction]. November 2012. http://ippog.web.cern.ch/resources/2011/cms-slice-july-2010-version.
20. The CMS Collaboration. The CMS experiment at the CERN LHC. *Journal of Instrumentation. 3:S*08004 (2008).
21. The CMS Collaboration. Energy resolution of the barrel of the CMS electromagnetic calorimeter. *Journal of Instrumentation. 2 (2007) P*04004. doi:10.1088/1748-0221/2/04/P04004 (2007).
22. G. Baiatian. Design, Performance and Calibration of CMS Hadron-Barrel Calorimeter. *CMS NOTE 2006 — 138.* arXiv:hep-ex/0007045.doi:10.1016/S0168-9002(00)00711-7 (2007).
23. THe CMS Collaboration. The CMS Particle Flow Algorithm. *Proceedings of the CHEF*2013 *Conference* (2013).
24. Particle Data Group Collaboration. Review of particle physics. *J. Phys. G 37* 075021 (2010).
25. Tau POG. Tau reconstruction and identification performance in run 2. *CMS Draft Analysis Note AN*-15-229 (24th Mai 2016).
26. The CMS Collaboration. Reconstruction and identification of tau lepton decays to Dhadrons and tau nneutrino at CMS. *JINST* 11 *P*01019 (February 2016).
27. Michael Brodski. MUSiC. *Model Unspecific Search in CMS with τ Leptons* MA thesis (RWTH Aachen, 2012).
28. W. Adam, R. Frühwirth, A. Strandlie & T. Todor. Reconstruction of Electrons with the Gaussian Sum FIlter in the CMS Tracker at the LHC. *CMS-NOTE*-2005-001 (2005).
29. A. Belyaev, N. D. Christensen & A. Pukhov. CalcHEP 3.4 for collider physics within and beyond the Standard Model. *Phys. Rev. Lett. 83 (1999) 3370.* arXiv:hep-ph/9803315. (1999).
30. T. Sjostrand, S. Mrenna & P. Z. Skands. A Brief Introduction to PYTHIA 8.1. *Comput. Phys. Commun.* 178(2008)852–867 (2008).
31. GEANT4 Collaboration. GEANT4: A Simulation toolkit. *Nucl. Instrum. Meth. A*506(2003)250–303. doi:10.1016/S0168 — 9002(03)01368 — 8 (2003).
32. J. Fernandez & C. D. Pardos. *TOP Trigger (Run2)* https://twiki.cern.ch/twiki/bin/view/CMS/TopTrigger. 21th July 2016.
33. A. Holtzner. *Egamma HLT in CMSSW* https://twiki.cern.ch/twiki/bin/view/CMSPublic/SWGuideEgammaHLT. 15th April 2011.
34. S. Harper & A. Randle-Conde. *HEEP Electron ID and isolation* https://twiki.cern.ch/twiki/bin/view/CMS/HEEPElectronIdentificationRun2. 15th May 2015.

35. A. Nayag. *TauID for 13 TeV run: recommendation from the Tau POG* https://twiki.cern.ch/twiki/bin/view/CMS/TauIDRecommendation13TeV. 24th June 2016.

36. The CMS Collaboration. Identification of b quark jets at the CMS Experiment in the LHC Run 2. *CMS-PAS-BTV*-15 – 001 (14th May 2016).

37. The CMS Collaboration. Search for lepton flavour violating resonant tau sneutrino production into a electron and muon in pp Collisions at $\sqrt{s} = 13$ TeV. *CMS AN*-15-191 (2016).

38. The CMS Collaboration. Measurement of the electron charge asymemtry in inclusive W production in pp collisions at $\sqrt{s} = 7$ TeV. *Phys. Rev. Lett.* 111806. (2012).

39. G. Cowan. *Statistical Data Analysis* (ed Press, C.) (Ser. Oxford science publications., 1998).

40. Higgs working group. *Higgs combined limit setting tool* [web page]. https://twiki.cern.ch/twiki/bin/view/CMS/SWGuideHiggsAnalysisCombinedLimit.

41. The ATLAS Collaboration. Search for a Heavy Neutral Particle Decaying to $e\mu$, $e\tau$, or $\mu\tau$ in pp Collisions at $\sqrt{s} = 8$ TeV with the ATLAS Detector. *PH-EP*-2015-028 (2015).

42. RWTH Aachen 3. Physikalisches Institut A. *Monte Carlo Samples Library* https://cms-project-aachen3a-datasets.web.cern.ch/cms-project-aachen3a-datasets/aix3adb2/?m=samples&a=indexmcsamples.

43. RWTH Aachen 3. Physikalisches Institut A. *Monte Carlo Skims Library* https://cms-project-aachen3a-datasets.web.cern.ch/cms-project-aachen3a-datasets/aix3adb2/.

If we knew what it was we were doing,
it would not be called research, would it?

— Albert Einstein

ACKNOWLEDGEMENTS

I would first like to thank Prof. Dr. Thomas Hebbeker, who gave me the opportunity to develop my thesis at his institute.

My interest into particle physics and the decision to develop a thesis about the CMS is due to Prof. Lutz Feld, who inspired me within his lectures and Dr. Christian Sturm, who waked my affection for physics during my insight at the GSI helmholtz center for heavy ion research.

I also want to thank all the colleges of the Institute 3A of the RWTH Aachen university for their collaboration. You supported me greatly and were always willing to help me. I would particularly like to single out my supervisor Mr. Sören Erdweg, I want to thank you for your excellent cooperation and for all the opportunities I was given to conduct my research and further my thesis.
In addition, I would like to thank Ms. Swagata Mukherjee for her valuable guidance and help. You definitely helped me to complete my thesis successfully.

I would also like to thank Jonas Lieb and Simon Knutzen for their wise counsel and sympathetic ear. You are always there for me. Finally, there is Isabelle Hirscher. Thank you for your lovely support during this time.

Thank you very much, everyone!

Alex Kreuzer

Aachen, July 13, 2016.